HHS Public Access

Author manuscript

Neuron. Author manuscript; available in PMC 2019 November 07.

Published in final edited form as:

Neuron. 2018 November 07; 100(3): 728–738.e7. doi:10.1016/j.neuron.2018.10.042.

Noninvasive ultrasonic drug uncaging maps whole-brain functional networks

Jeffrey B. Wang[#1,2], **Muna Aryal**[#1,2], **Qian Zhong**[1], **Daivik B. Vyas**[1], and **Raag D. Airan**[1,3,*]

[1]Department of Radiology, Neuroradiology Division, Stanford University, Stanford, CA 94305, USA

[2]These authors contributed equally

[3]Lead Contact

[#] These authors contributed equally to this work.

Summary

Being able to noninvasively modulate brain activity, where and when an experimenter desires, with an immediate path towards human translation is a long-standing goal for neuroscience. To enable robust perturbation of brain activity while leveraging the ability of focused ultrasound to deliver energy to any point of the brain noninvasively, we have developed biocompatible and clinically-translatable nanoparticles that allow ultrasound-induced uncaging of neuromodulatory drugs. Utilizing the anesthetic propofol together with electrophysiological and imaging assays, we show that the neuromodulatory effect of ultrasonic drug uncaging is limited spatially and temporally by the size of the ultrasound focus, the sonication timing, and the pharmacokinetics of the uncaged drug. Moreover, we see secondary effects in brain regions anatomically distinct from and functionally connected to the sonicated region, indicating that ultrasonic drug uncaging could

[*]Correspondence: Raag D. Airan MD PhD, rairan@stanford.edu.

Author contributions:

JBW, MRA, QZ, and RDA designed the experiments. JBW implemented the EEG hardware, wrote the EEG acquisition and analysis software, wrote the PET analysis software, and completed the EEG and PET data analysis. MRA completed the EEG experiments, including parameter optimization for the *in vivo* uncaging experiments, and completed the safety studies with MRI and histological endpoints. MRA and JBW implemented and calibrated the ultrasound systems, including characterizing the ultrasound fields *in vivo*. QZ produced the nanoparticles and completed their physicochemical characterization and *in vivo* particle kinetics and biodistribution analysis. JBW and DBV completed the PET experiments. JBW, MRA, and RDA wrote the paper and generated the figures, with input from all the authors.

Conceptualization: RDA, MRA, JBW, QZ. *Methodology:* JBW, MRA, QZ, RDA. *Software*: JBW. *Validation*: MRA, JBW, QZ, RDA. *Formal Analysis*: JBW, QZ. *Investigation*: JBW, MRA, QZ, DBV. *Resources*: QZ, MRA, JBW, RDA. *Data Curation*: JBW. *Writing – Original Draft*: JBW, MRA, RDA. *Writing – Review & Editing* : JBW, MRA, QZ, DBV, RDA. *Visualization*: JBW, MRA, QZ, RDA. *Supervision*: RDA. *Project Administration:* RDA. *Funding Acquisition*: RDA.

Declaration of interests: Patent applications have been filed on the nanoparticles described in this manuscript (17–163 – Provisional application w ith Stanford University; QZ and RDA) and on related technology (PCT/US2017/033226 with Johns Hopkins University; RDA).

Data and materials availability: All relevant data is available in the main text or supplementary materials. Analysis code and further methodological details and protocols will be made available within a reasonable time frame upon request.

Data and Software Availability

All data and code are available upon reasonable request to Raag D. Airan (rairan@stanford.edu).

noninvasively map the changes in functional network connectivity associated with pharmacologic action at a particular brain target.

eTOC

Wang, Aryal, *et al.* demonstrate that nanoparticle-mediated ultrasonic drug uncaging noninvasively modulates brain activity with precision determined by the ultrasound focus extent and the kinetics of the uncaged drug, and establish that this technology can causatively map whole-brain functional networks.

Keywords

Focused Ultrasound; Neuromodulation; Functional Imaging; Functional Connectivity; Nanotechnology; Drug delivery

Introduction

Realizing novel techniques for improved control of the human nervous system is a key goal of the neuroscience community (Jorgenson et al., 2015). The ideal neuromodulatory technique would allow noninvasive manipulation of any part of the brain with high spatial and temporal precision. It would flexibly allow control over any of the varied modes of communication in the brain, including excitatory, inhibitory, and modulatory inputs. Importantly, it would have a short and straightforward path to safe and effective use in wild-type large animals and humans.

We recently proposed accomplishing these objectives with ultrasonic drug uncaging, in Which noninvasive neuromodulation is accomplished by using ultrasound to uncage neuromodulatory drugs from nanoparticle drug carriers (Airan, 2017). Focused ultrasound is a near-ideal modality to noninvasively transmit energy to the brain, given that ultrasound systems currently in clinical use can sonicate the central brain transcranially with spatial and temporal precision on the order of millimeters and milliseconds (Ghanouni et al., 2015; Lipsman et al., 2014). Additionally, polymeric nanoscale emulsions of perfluorocarbons have been used as ultrasound-mediated delivery vehicles for chemotherapeutics (Fabiilli et al., 2010; Rapoport, 2016; Sheeran and Dayton, 2012; Sheeran et al., 2016). Previously, we adapted these nanoparticles to a biocompatible formulation that allows encapsulation and uncaging of the small molecule anesthetic propofol (Airan et al., 2017), a potent GABA(A) agonist, and designed these nanoparticles to be composed of ingredients that are each approved for human administration in different contexts (Makadia and Siegel, 2011; Robbin and Eisenfeld, 1998). However, until now there has been no demonstration that ultrasonic drug uncaging could indeed capitalize on the principal attractive features of focused ultrasound for neuroscience: noninvasive localization in space and time without physical constraints on the depth of penetration. Here, we deliver on that promise by demonstrating for the first time that the neuromodulation induced by ultrasonic propofol uncaging is indeed limited by the spatial and temporal extent of sonication and the pharmacokinetics of the uncaged drug. We further demonstrate the power of this technique for neuroscientific inquiry by showing that ultrasonic drug uncaging drives secondary changes in brain regions that are

functionally connected to the sonicated target, thereby mapping the network-level changes in functional connectivity induced by a localized pharmacologic stimulus.

Results

Drug-loaded Nanoparticles Uncage Propofol upon Sonication Efficaciously and Safely

In the envisioned application, drug-loaded ultrasound-sensitive nanoparticles would be intravenously administered and then uncaged with ultrasound while in the intravascular blood volume of the target brain region. The drug would then diffuse across the intact blood-brain barrier to act on the sonicated brain (Fig. 1A). We optimized these nanoparticles for ultrasonic drug uncaging with sub-megahertz ultrasound frequencies, to match the frequencies used for clinical transcranial sonication (Ghanouni et al., 2015; Hynynen and Jolesz, 1998; Lipsman et al., 2014, 2018). Importantly, compared to prior formulations (Airan et al., 2017; Rapoport, 2012), our current nanoparticles showed improved monodispersity, stability, drug loading, and free drug fraction (Fig. 1B; typical dynamic light scattering results of Z-averaged diameter 397.3 ± 10.0 nm, with polydispersity index 0.068 ± 0.023, zeta potential −26.7 ± 0.6 mV, and drug loading of 1.19% of nanoparticle weight). These nanoparticles uncaged propofol with an estimated *in vitro* pressure dose-response inflection at 0.8 MPa with 650 kHz sonication, with uncaging efficacy increasing with both sonication pressure and burst length (Fig. 1C). In circulation, the nanoparticles cleared from the blood with a dual-exponential profile with estimated half-lives of 12.6 and 91.4 min for each exponential (Fig. 1D), with no detectable nanoparticles in circulation 24 h after administration. At 24 h after administration, the nanoparticles were primarily sequestered in the liver, with less uptake in the spleen and lungs, minimal uptake in the kidney and heart, and importantly, no evidence of nonspecific binding to the brain (Fig. 1E). Furthermore, the brains of animals that underwent focused sonication using maximal sonication pressure and maximal duty cycle (650 kHz sonication; 60 × 100 ms bursts with 1 Hz burst repetition frequency, 1.8 MPa peak *in situ* pressure) following nanoparticle administration (10 min following bolus administration of 1 mg/kg of encapsulated propofol) showed no evidence of acute injury or blood-brain barrier disruption by either histology or contrast-enhanced MRI (Figs. 1F, S1A). Additionally, there was no evidence of parenchymal damage in animals receiving repeated nanoparticle dosing and sonication, up to nine times over several weeks. Indeed, we have seen no evidence of nanoparticle or sonication-related toxicity in any of the >100 rats that have undergone ultrasonic drug uncaging using these nanoparticle concentrations and with these sonication parameters. These results together show that this nanoparticle formulation allows safe and effective ultrasonic drug uncaging, with practical sonication dose-response relationships and *in vivo* particle kinetics.

Ultrasonic Propofol Uncaging Reversibly Silences Visual Evoked Potentials

To assess the spatial and temporal resolution of neuromodulation with this technique, we first noted the limited diffusion in brain tissue (Gredell et al., 2004) and rapid kinetics of action (Upton and Ludbrook, 1997) of the anesthetic propofol. We quantified the temporal kinetics of anesthetizing visual evoked potentials (VEPs) with ultrasonic propofol uncaging directed to the primary visual cortex (V1; Fig. 2A). In all experiments of this current study, animals received a total dose of 1 mg/kg of encapsulated propofol. At that dose, free

propofol given intravenously as a bolus is insufficient to affect VEP amplitudes (Fig. 2B). Nonetheless, ultrasonic propofol uncaging directed to V1 markedly attenuated this physiologic activity, with a decrease of the N1P1 amplitude commencing with sonication, and rapid recovery of this amplitude seen in the immediate post-sonication period (Fig. 2C, left). Furthermore, neither this sonication protocol alone nor nanoparticle administration itself significantly affected the N1P1 VEP amplitude (Fig. 2C, middle). This effect was limited to the sonication period and showed a dose-response relationship with each of the applied sonication pressure and the burst length (Figs. 2C, right, 2D, left and middle), consistent with the *in vitro* uncaging results (Fig. 1C). Interestingly, at 1.8 MPa, at the end of sonication, we observed an increase in VEP amplitude relative to baseline in some animals, potentially due to post-inhibitory rebound spiking (Nortmann et al., 2015; Sanchez-Vives et al., 2000). Notably, this phenomenon has been observed previously with optogenetic halorhodopsin inhibition (Yang et al., 2018) and also has been hypothesized *in silico* to underlie the paradoxical excitatory action of subanesthetic doses of propofol (McCarthy and Kopell, 2012).

Recognizing recent findings that neuromodulation from focused ultrasound can arise primarily from an indirect auditory response (Guo et al., 2018; Sato et al., 2018), we conducted the same sonication protocol with non-drug-loaded blank nanoparticles. We found that blank nanoparticles yielded no effect, indicating that the observed neuromodulation is specific to propofol uncaging, and not a result of the sonication itself nor the other nanoparticle constituents.

To investigate whether this anesthesia was specific to sonication of V1, we sonicated the motor cortex (M1; Fig. 2A, right) as a target that is both spatially and functionally separated from the visual system. Furthermore, as there is little arterial communication between the two hemispheres in the rat brain (Lee, 1995), we opted to sonicate the M1 cortex ipsilateral to the investigated V1 and contralateral to the light stimulus to assess for any nonspecific effects due to released propofol spreading by perfusion or diffusion. As predicted, sonication of this target showed no such attenuation of the N1P1 VEP amplitude (Fig. 2D, right). We further found that sonication of a target encompassing part of the lateral geniculate nucleus (LGN; Fig. 2A, right) was also able to significantly attenuate the VEP amplitude (Fig. 2D, right), suggesting that ultrasonic propofol uncaging could yield secondary effects in regions functionally downstream of the sonicated target. Notably, this effect is smaller than direct propofol uncaging in V1 likely because our focus spot size only encompassed part of the LGN while also encompassing non-LGN regions. The temporal kinetics of these effects showed half-lives of 8–15 sec (Figs. 2E, S2), correlating well with the known pharmacokinetics of propofol action (Upton and Ludbrook, 1997), and indicating that the temporal kinetics of this technique are determined by the timing of sonication and the pharmacokinetics of the uncaged drug. Together these results show for the first time that ultrasonic drug uncaging may noninvasively and reversibly modulate physiologic brain activity, with dose-response relationships with the applied sonication parameters *in vivo*, and with a temporal extent that is determined by the timing of sonication and the pharmacokinetics of the uncaged drug.

Ultrasonic Propofol Uncaging Induces Spatially Localized Anesthesia

To more fully assess the spatial profile of the anesthesia induced with ultrasonic propofol uncaging, we turned to functional brain imaging. Specifically, we used positron emission tomography (PET) imaging of the uptake of [18F]-fluorodeoxyglucose (FDG), a glucose analog, with a relative decrease in FDG avidity indicating effective anesthesia induced by the uncaged propofol (Tasbihgou et al., 2018). Given the low rate of diffusion for propofol within the brain (Gredell et al., 2004), the spatial extent of the anesthesia induced by ultrasonic propofol uncaging would be determined by the extent of parenchyma whose perfusion is supplied by the vessels in which the nanoparticles are uncaged. As rodent cortical parenchyma is supplied by penetrating arteries extending radially inward from the outer cortical surface (Xiong et al., 2017), sonication near the cortical surface would likely yield the broadest spatial extent of the effect and, therefore, the worst spatial resolution of the technique. To establish a worst-case bound of this spatial resolution, we therefore targeted the sonication focus (650 kHz, 240 × 50 ms bursts, with 1 Hz burst repetition frequency) to the cortical surface, with the majority of the focus in the rat dorsal primary motor cortex, and with the far field of sonication entering the dorsal hippocampus (Fig. 3A, left; *in vivo* mapping of the maximal sonication extent in Fig. S1B). Indeed, following propofol-loaded nanoparticle administration, during sonication with 1.2 MPa peak *in situ* pressure, a robust decrease in FDG avidity was visualized precisely within the full-width at half-maximum (FWHM) profile of the sonication focus, exactly at the sonication target (Fig. 3A, right). This neuromodulation was reliably visualized across this cohort (Figs. 3D-E, S3A). This decrease in avidity was not seen with blank nanoparticles, indicating that this effect is specific to propofol uncaging and not driven by sonication itself nor the other nanoparticle constituents. As with VEP attenuation (Fig. 2), this effect was limited to the time period of sonication (Fig. 3B). With 1.8 MPa sonication, the magnitude of the decrease of FDG avidity was unchanged (Fig. 3C), but the spatial extent of the affected region increased (Fig. 3A, right, 3E-F). This spatial extent at 1.8 MPa was still within the sonication FWHM, corresponding to the dose-response relationship of propofol uncaging and sonication pressure seen *in vitro* (Fig. 1C) as well as *in vivo* with VEP attenuation (Fig. 2D). Notably, increasing the sonication pressure by 50% (1.8 MPa vs. 1.2 MPa) increased the effect FWHM by 44% (Fig. 3F), as would be expected from the rectified linear pressure dose-response relationship that is implied by our *in vitro* results (Fig. 1C). Comparing the spatial extent of the anesthetic decrease in FDG avidity with the expected sonication profile *in situ*, an effective *in vivo* threshold of approximately 1.0 MPa with 650 kHz sonication was estimated for the localized anesthesia induced by ultrasonic propofol uncaging.

Ultrasonic Propofol Uncaging Induces Secondary Anesthesia of a Functionally Connected Network

Next, we noted qualitatively that with 1.8 MPa sonication, in addition to the primary decrease of FDG avidity seen in the sonicated target, there appeared to be other sites spatially distinct and separated from the sonication target showing apparent decrease in FDG avidity, albeit to a lesser extent (Fig. 3A, right). To assess the consistency of this observation, the imaging volumes from animals receiving cortical sonication of 1.8 MPa peak negative pressure were coregistered to each other. Statistical parametric maps were calculated across the whole brain for the z-scores of the difference in FDG avidity of a given

voxel between the sonication time period and a delayed time-period at the end of the PET acquisition (Fig. 4A). These maps were then thresholded at the false-discovery rate (FDR), to account for multiple statistical comparisons in this whole-brain analysis. While no brain voxels showed a significant difference of FDG avidity during cortical target sonication of blank nanoparticle treated animals (Fig. 4B, top), a substantial number of brain voxels for propofol nanoparticle treated animals did show such a difference with sonication at 1.8 MPa (Fig. 4B, bottom), but notably not at 1.2 MPa or with sham sonication (Fig. S4A). These sites were spatially distinct and separated from the sonication target, with some even in the contralateral brain. These foci localized primarily to the ipsilateral more than contralateral thalamus (Bosch-Bouju et al., 2013) and hippocampus (Hess et al., 1995), with additional sites of functional decrease localizing to the tectum (Rubelowski et al., 2013), and the ipsilateral olfactory bulb and cortex (Cinelli et al., 1987; Van Groen and Wyss, 1990). Interestingly, we found that all voxels that showed significance beyond the FDR had less metabolic activity associated with the cortical uncaging of propofol. This is in line with previous studies identifying that the majority of projection neurons of the cortex are excitatory (Spruston, 2008). The lack of significant voxels at the primary sonication target at 1.2 MPa is likely due to the effect spatial size being on the order of a single voxel, the inevitable small differences in experimental targeting, and that the whole-brain coregistration process translated these small deviances to yield no substantial overlap of the sonicated areas in these whole-brain coregistered and averaged images (Fig. S5A). In contrast, at 1.8 MPa, the spatial size of the effect was large enough for the anesthetized areas to overlap, resulting in statistically significant voxels at the sonication target (Fig. S5B).

To validate that this analysis was indeed assessing changes in functional connectivity, we noted the significant bidirectional interconnectedness of the central thalamus and frontal cortex (Brown et al., 2011) and the secondary decrease in central thalamic metabolism with frontal cortical propofol uncaging (Fig. 4B). We decided to assess propofol uncaging in the central thalamus under the hypothesis that this intervention should yield a corresponding decrease of activity in the frontal cortex, as an inverse of what has been seen with optogenetic activation of this region (Liu et al., 2015) and to test the efficacy of ultrasonic propofol uncaging to noninvasively modulate this deep brain region. Overall, we expected that deep subcortical structures such as the thalamus would likely show an even greater extent of functional connectivity across the brain (Brown et al., 2011) compared to cortical sonication. A sonication target centered on the paracentral and mediodorsal nuclei of the thalamus was chosen (Fig. 5A, left; *in vivo* mapping of the maximal sonication extent in Fig. S1B), with the transducer sonication profile extending dorsally into the dorsal hippocampus and ventrally into the hypothalamus. As with the cortical target, with ultrasonic propofol uncaging in this deep target, a robust decrease in FDG avidity was seen within the sonication target, which was spatially restricted to the sonication focus, with no such effect in animals receiving blank nanoparticles (Fig. 5A–B). The same functional connectivity analysis that was used for the cortical sonication data was then applied to the deep sonication data. Indeed, while blank nanoparticle-treated animals showed no such change in functional connectivity during deep sonication (Fig. 5C, top), a whole-brain network of activity changes was seen with ultrasonic propofol uncaging in the deep target, with these changes principally localized to the ipsilateral more than contralateral frontal, prefrontal, and insular

cortices (Brown et al., 2011; Liu et al., 2015), the olfactory bulbs and cortex (Courtiol and Wilson, 2014), and the midbrain (Brown et al., 2011; Heckers et al., 1992) (Fig. 5C, bottom). All statistically significant voxels were inhibited during propofol uncaging in this deep target, agreeing with previous studies establishing that central thalamic projection neurons are primarily excitatory (Ellender et al., 2013).

Discussion

Overall, we have seen that these ultrasound-sensitive nanoparticles have desirable physicochemical properties and drug loading, show suitable ultrasonic uncaging efficacy *in vitro*, and are well tolerated by rats (Figs. 1, S1). We observed that ultrasonic propofol uncaging can selectively attenuate visual evoked potentials when targeting regions in the visual pathway, with a temporal resolution of approximately ten seconds with respect to the sonication timing (Figs. 2, S2), consistent with the known pharmacokinetics of propofol action (Upton and Ludbrook, 1997). Using FDG PET, we observed that ultrasonic propofol uncaging induced silencing of the brain that was limited to the sonication field (Figs. 3, S3) and that, with higher ultrasound intensities, secondary changes were induced in regions functionally connected to the sonication target (Figs. 4, 5, S4, S5), creating functional connectivity maps of the network effects of localized propofol action. These results together demonstrate that ultrasonic drug uncaging can be used not only for spatially and temporally localized drug delivery, but also for mapping the brain network-level physiological responses to localized pharmacologic action.

We have also validated that these nanoparticles may encapsulate and uncage a wide variety of drugs, so long as they are lipophilic, including ketamine, dexmedetomidine, and nicardipine (Zhong et al., 2018). As lipophilicity is a hallmark of drugs that naturally may cross the blood-brain barrier (Chen and Liu, 2012), ultrasonic drug uncaging from these nanoparticles is particularly suited for the delivery of neuromodulatory drugs. Given its limited diffusion in the brain (Gredell et al., 2004) and short time of action (Upton and Ludbrook, 1997), propofol may be taken as a model drug to define the spatial and temporal resolution of ultrasonic drug uncaging more generally. Certainly, given the estimated diffusion coefficient of propofol of 0.02×10^{-6} cm^2 s^{-1} (Gredell et al., 2004) and an estimated capillary transit time of 1.4 s (Jespersen and Østergaard, 2012), we estimate the extent of diffus ion beyond the capillary bed during this transit time to be only 1.7 μm, suggesting that perfusion-related effects dominate in the distribution of propofol following uncaging. Indeed, the results presented here (2, 3) suggest that the resolution of ultrasonic drug uncaging is defined principally by the spatiotemporal extent of sonication and the action of the particular drug that is uncaged. Even with a more volatile agent such as halothane, which has an order of magnitude faster diffusion coefficient (Chesney et al., 2003), we estimate the extent of diffusion to be only up to 11 μm during capillary transit, indicating that this result and model should hold generally for a wide range of drugs with different rates of transport within the brain.

The relatively restricted spatial extent of these effects is an important surprising and welcome feature, given the potential for vascular perfusion to carry the uncaged drug beyond the sonication focus. Regarding this point, we first note that uncaged drug will enter the

brain parenchymal compartment primarily at the capillary level, the typical site for blood-parenchyma solute exchange (Upton, 2007). Also, the typical linear extent of brain parenchymal transit of an agent within the tortuous capillary bed is only 150–500 μm (Hudetz, 1997). Additionally, even if there is significant diffusion of the drug within the brain parenchyma, dilution of the drug into the volume of diffusion would lower the effective drug concentration and limit the diffusion-related spread of drug action. We would therefore expect that the maximal spatial extent of the action of ultrasonically uncaged drug would be less than ~0.5 mm beyond the brain region that is sonicated with a pressure that is above the effective uncaging threshold (1.0 MPa for propofol uncaging with 650 kHz sonication; Figs. 1–3).

It is unlikely for the results of the functional connectivity mapping analysis (Figs. 4, 5) to be confounded by effects of diffusion or perfusion given the considerations noted above. Furthermore, given the contiguous nature of arterial blood supply and the lack of arterial communication across hemispheres (Lee, 1995), diffusion or perfusion confounds should result in statistically significant modulations of voxels that are interconnected and do not cross into the contralateral brain. In contrast, we observe that the secondary sites of uncaged propofol-induced changes are multiple, discrete, unconnected, and even in the contralateral brain (Figs. 4, 5), highlighting that the observed changes are unlikely to represent perfusion or diffusion confounds. Also, temperature changes are unlikely to be responsible for this neuromodulation, given that with these sonication protocols (i.e. 50 ms bursts at 1.8 MPa or 100 ms bursts at 1.2 MPa), each sonication burst would result in an estimated temperature increase of ~0.1 °C (calculations detailed in STAR Methods)(Azhari, 2010; ter Haar and Coussios, 2007; Hasgall et al., 2015; Nyborg, 1988). This temperature change would rapidly dissipate during the 900–950 ms of time for which the transducer is not active in each period, indicating that there should be no accumulated thermal dose.

Simulation studies have suggested that there may be minimal off-target sonication of substantial intensity due to scatter during focused ultrasound transmission in small rodent skulls (Younan et al., 2013), serving as a potential confound. However, the *in vivo* spatial profile of sonication in our work is restricted to the sonication trajectory and does not directly overlap with these functional maps (Figs. 4, 5, S1B), in agreement with other *in vivo* characterizations of similar sonication fields in rat skulls (McDannold et al., 2013; O'Reilly et al., 2010). It is therefore unlikely that scatter of the ultrasound would yield the variety of distant discrete foci that we observe in our functional connectivity maps, especially given that: there was a lack of similar effects seen with 1.2 MPa sonication (Fig. S4A); the scattered ultrasound would likely be of lower intensity than that in the primary sonication target; and targeting different sites a few millimeters apart yielded wholly different functional signatures (Fig. 4B, 5C). We do note that our spatial analysis may be limited by the inevitable likelihood of standing wave generation (O'Reilly et al., 2010) with sub-megahertz sonication in small rodent skulls. A more complete analysis will likely necessitate the use of larger animal models whose cranial vaults are significantly larger than the spatial length of the applied ultrasound pulses in tissue. Indeed, the main limitation of this work is that current small animal focused ultrasound systems generally have foci that are broad longitudinally to the point of spanning the entire dorsal-ventral axis of the brain (Fig. S1B). Future work with this system in small animals will depend on the development of ultrasound

transducers with smaller focal spot sizes and that are ideally wearable to allow awake, behaving analyses (Lee et al., 2018; Sieu et al., 2015; Tiran et al., 2017; Urban et al., 2015). Furthermore, the use of multi-element transducers that could surround the cranium would allow for tighter focal lengths in the longitudinal direction (Ghanouni et al., 2015; Lipsman et al., 2014).

Given its temporal resolution defined by the ultrasound timing and drug pharmacokinetics (Fig. 2), spatial resolution defined by the ultrasound focus (Fig. 3), and versatility for delivering a wide range of lipophilic compounds (Zhong et al., 2018), noninvasive neuromodulation using ultrasonic drug uncaging offers complementary features to other techniques for neuromodulation. With localized drug application, ultrasonic drug uncaging could add a pharmacological adjunct to either invasive (Bichot et al., 2011; Leuchter et al., 2012; Mayberg et al., 2005) or noninvasive (Allan et al., 2012; Farzan et al., 2016; Grossman et al., 2017; Vöröslakos et al., 2018) electromagnetic neurostimulation or direct ultrasound neuromodulation techniques (Casella et al., 2017; Chaplin et al., 2018; Deffieux et al., 2013; Guo et al., 2018; King et al., 2013; Lee et al., 2015; Legon et al., 2014; McDannold et al., 2015; Sato et al., 2018; Tyler et al., 2018; Ye et al., 2016). To enable clinical translation, these nanoparticles are by design composed of ingredients that are each approved for human administration in different contexts (Makadia and Siegel, 2011; Robbin and Eisenfeld, 1998), and their application does not appear to disrupt the blood-brain barrier (Fig. S1A) or otherwise adversely impact the brain (Fig. 1). Ultrasonic drug uncaging could therefore be readily translated and applied in larger wild-type animals, and potentially in humans, to test hypotheses generated by other neuromodulatory techniques that, for example, genetically modify the brain (Chen et al., 2015; Ibsen et al., 2015; Lee et al., 2014; Szablowski et al., 2018; Zhang et al., 2010). Future studies will work towards this large animal and clinical translation, will map changes in the functional connectome induced by focal pharmacologic perturbation (Figs. 4, 5), and will also determine the potential behavioral changes associated with ultrasonic drug uncaging within different brain regions and with a variety of neuromodulatory drugs.

STAR METHODS

Contact for Reagent and Resource Sharing

Further information and requests for resources and reagents should be directed to and will be fulfilled by the Lead Contact Raag D. Airan (rairan@stanford.edu).

Experimental Model and Subject Details

All experiments described in this work involving vertebrate animals were approved under the Stanford Administrative Panel on Laboratory Animal Care (APLAC), protocols 22100 and 32874, conforming to institutional and national guidelines and regulations. In this work, healthy wild-type male Long-Evans rats (6–15 weeks old) were used. Subjects were not previously used for any other procedures. For EEG recordings and PET experiments, animals were used for multiple recording or imaging sessions, with at least 48 hours between each session. For the blood-barrier opening experiments used to visualize the sonication field, each animal was used once. Unless stated otherwise, rats were housed in

cages with 2–3 inhabitants, with a day-night cycle enforced from 7 AM-7 PM. Animal husbandry was provided by veterinarians and technicians at the Stanford Veterinary Services Center (VSC). Food and water were freely available, unless otherwise stated.

Method Details

Nanoparticle synthesis and characterization

Chemicals: Di-block copolymers are made up of a hydrophilic block of polyethylene glycol (PEG; mol. wt. 2 kDa) and a hydrophobic block of poly(lactic-co-glycolic acid) (PLGA). Two molecular weights of hydrophobic block chains were used: 2 kDa and 5 kDa. The example of nomenclatures for di-block copolymer is polyethylene glycol 2 kDa - poly(lactic-co-glycolic acid) = PEG (2 kDa)-PLGA (5 kDa). All di-block copolymers were purchased from Akina (West Lafayette, IN, USA). Propofol was purchased from Alfa Aesar (Haverhill, MA, USA). Ketamine hydrochloride injectable solution is a controlled substance and was purchased via Stanford University Environmental Health & Safety. Tetrahydrofuran (THF) and hexane were obtained from Sigma-Aldrich (St Louis, MO, USA). n-Perfluoropentane (PFP) was purchased from FluoroMed (Round Rock, TX, USA). A hydrophobic IRDye® 800RS infrared dye was purchased from LI-COR Biotechnology (Lincoln, NE, USA).

Production of Nanoparticles: 150 mg of di-block copolymer and 15 mg of propofol were combined in a 20 ml glass beaker and 10 ml THF was added to dissolve the polymer and drug. Then, 10 ml of phosphate buffer saline (PBS) was added dropwise to the organic solution over 5 min. The THF was fully evaporated by placing the mixture overnight in atmosphere and then in vacuum for 1 h. This produced drug-loaded polymeric micelles in saline suspension. Then, 300 μl cold PFP was added to the suspension, followed by 5 min sonication in a 40 kHz Bransonic M1800H bath sonicator (Thermo Scientific; Waltham, MA, USA) which was pre-filled with iced water. The solution was centrifugated at 4 °C at 2000 g for 10 min. The sup ernatant was decanted and the resulting pellet was resuspended in cold PBS. Centrifugation-resuspension was repeated two more times to remove and dilute residual free drug, polymer, and PFP-free micelles. Finally, the nanoemulsion suspension was extruded twice using an Avestin Liposofast LF-50 extruder (Ottawa, ON, Canada) equipped with compressed nitrogen (40 psi) and loaded with a polycarbonate membrane of 0.6 μm pores. The extruded nanoemulsion suspensi on was either used fresh or mixed with glycerin (2.25%, w/v) as a cryoprotectant, frozen immediately, and stored at −80 °C until it was thawed for use.

Characterization of Nanoparticles: The Z-average diameter, polydispersity index (PDI) and zeta potential of the drug-loaded phase-change nanoemulsions were measured via dynamic light scattering (DLS) with a Malvern Zetasizer Nano ZS90 (Malvern, United Kingdom). A 10 μl nanoemulsion solution was thoroughly mixed with 990 μl cold PBS. DLS paramete rs were: materials = perfluoropentane; Refractive Index (RI) = 1.330; absorption = 0.1; dispersant = ICN PBS tablets; viscosity = 0.8882 cP at 25 °C; Mark-Houwink parameters; equili bration time = 60 s; disposable cuvettes = ZEN0118; measurement angle = 90 degree; measurement duration = automatic; number of measurements = 5; positioning method = seek optimum position; analysis model = general

purpose (normal resolution). To measure the zeta potential, 10 μl nanoemulsion solution was mixed with 990 μl deionized water. Then 900 μl of t his solution was transferred to a disposable capillary cell. Measurement parameters were: cell type = DTS1070, dispersant = water; viscosity = 0.8872 cP at 25 °C; dielectric constant = 78.54; F(κa) selection model = Smoluchowski; F(κa) value =1.5; measurement duration = automatic; measurement runs between 10 and 100; number of measures = 3 with no delay between measurements.

Quantification of Nanoparticle Drug Loading: A 100 μl nanoemulsion solution was thoroughly mixed with 900 μl methanol. The fluorescence of propofol was quantified with a Tecan Infinite M1000 microtiter plate reader (San Jose, CA, USA) at excitation/emission = 276/302 nm. The propofol content was calculated with respect to a standard curve of propofol prepared in varying concentrations in the same solvent.

In Vitro Assay of Ultrasonic Drug Uncaging: A 50 μl nanoemulsion suspension (1 mg/ml drug equivalent) was added to a Fisherbrand™ 0.2 ml PCR tube (Fisher Scientific). 150 μl of hexa ne was added atop the nanoemulsion suspension. The PCR tube was placed in a custom holder and coupled using degassed water to a focused ultrasound (FUS) transducer (Image Guided Therapy, Pessac, France) at room temperature, such that the FUS focus was contained within the nanoemulsion suspension layer. The nanoemulsions were sonicated with FUS for 60 s total, with varying peak negative pressure and burst length, with a burst repetition frequency of 1 Hz. While varying pressure, the burst length was 50 ms; while varying burst length, the peak in situ pressure was 1.2 MPa. The center frequency of the transducer was 650 kHz. Following FUS, 100 μl of the organic phase was collected without disturbing the aqueous layer. The amount of the uncaged drug was quantified by measuring its UV fluorescence and comparing to a standard curve of the drug prepared in varying concentrations in hexane.

Pharmacokinetics of Nanoparticles: All animal experiments were carried out in accordance with the Stanford IACUC. Long-Evans rats with body weight 180–200 g (Charles River Laboratories, Wilmington, MA, USA) Were used in all *in vivo* studies. Propofol-loaded PFP/PEG (2 kDa)-PLGA (5 kDa) nanoemulsions were doped with a hydrophobic near-infrared fluorescent dye, IR800 (LI-COR, Lincoln, NE), during nanoemulsion production and then used to test *in vivo* blood-pool particle kinetics and systemic biodistribution.

To produce dye-doped nanoemulsions, 1 mg IR800 dye was added to the drug and polymer THF solution, and the rest of the nanoemulsion production protocol was unchanged. For the *in vivo* experiments, a nanoemulsion bolus (equivalent to 1 mg/kg of drug) was administered intravenously via a 24 g × 3/4” catheter paced in t he rat tail vein in a total volume of ~0.4–0.5 ml (N=3). Blood samples were collected via either left or right submandibular vein at 2 min 10 min, 20 min, 40 min, 2 h and 4 h, alternating sides for each sampling. The blood was split into two volumes. Whole blood sample fluorescence was assessed using a Lago (Spectral Instruments Imaging; Tucson, AZ, USA) imaging system (excitation/emission = 770/810 nm) and quantification was completed using regions of interest (ROIs) of the same size across samples, drawn within the capillary tube. The second volume of each sample was centrifugated in a microcentrifuge for a total of 10 min at 10,000 g at 4 °C. The plasma

fraction from these samples was then collected and their fluorescence was quantified in a similar fashion to that of whole blood samples. The nanoemulsion concentration in the whole blood and plasma were fitted with a two-compartment kinetic model, described in the next section.

For systemic biodistribution quantification, the same dye-doped propofol-loaded nanoemulsions were administered intravenously as a bolus to Long-Evans rats (N=3). The rats were sacrificed at 24 h post administration to harvest major organs: heart, liver, lungs, kidneys, spleen, and brain. These organs were imaged for IR800 fluorescence (excitation/emission=770/800 nm) using a Lago imaging system (Tucson, AZ) and quantified using regions of interest (ROI) of the same size, drawn to be within the image of each organ. The distribution of the nanoemulsion among the organs was calculated by dividing the ROI fluorescence of each tissue by the sum of ROI fluorescence values of all organs.

Modeling Pharmacokinetic Data: For modeling, we use the two-compartment model

$$\dot{x}_c(t) = k_{21}x_p(t) - \left(k_{el} + k_{12}\right)x_c(t)$$
$$\dot{x}_p(t) = k_{12}x_c(t) - k_{21}x_p(t),$$

where $x_c(t)$ and $x_p(t)$ are the nanoparticle concentration in the central blood pool and periphery, respectively, k_{12} and k_{21} are the rate constants for drug transfer from the blood pool to the periphery and vice-versa, and k_{el} is the elimination rate constant. Solving this equation by ansatz gives us a solution consisting of the double exponential of the form

$$x_c(t) = A_c e^{-r_d t} + B_c e^{-r_e t}$$
$$x_p(t) = A_p e^{-r_d t} + B_p e^{-r_e t},$$

where r_d is the rate of distribution and r_e is the rate of elimination (not to be confused with the elimination rate constant), and A_c/A_p and B_c/B_p are the coefficients for the distribution and elimination exponential phases, respectively. Note that our pharmacokinetics experiments primarily measure $x_c(t)$. Whole blood data contains contributions from both nanoparticles and micelles, whereas plasma contains contributions from micelles (and likely minimal free dye).

Histology: A total of ten animals were used to evaluate the histological effects of ultrasonic drug uncaging. Following nanoparticle administration and sonication, the animals were deeply anesthesized with ketamine/xylazine, and sacrificed and fixed via transcardial perfusion (0.9 % NaCl, 100ml: 4% paraformaldehyde, 250ml). The brains were then removed, embedded in paraffin, and serially sectioned at 4 μm in the transverse plane (perpendicular to the direction of ultrasound beam propagation). Every 50th section (200 μm apart) was stained with hematoxylin and eosin (H & E) and inspected using NanoZoomer-XR (Hamamatsu Photonics, Bridgewater, NJ), in consultation with a veterinary pathologist of the Stanford Veterinary Service Center.

Magnetic Resonance Imaging for Safety of Nanoparticles: For evaluating safety, a transmit/receive surface coil (diameter/radius of curvature: 4/3 cm) was placed above the rat head, and the system was placed in an animal 3T MRI (preclinical cryogenic-free, MR Solutions, Guildford, UK). Before and after ultrasonic propofol uncaging (1.8 MPa in situ pressure, 60 × 100 ms bursts delivered with 1 Hz burst frequency after intravenous administration of 1 mg/kg encapsulated propofol) in visual cortex, axial T2-weighted fast spin-echo (FSE) images (parameters: repetition time (TR): 5475 ms; echo time (TE): 68 ms; matrix size: 256×256; slice thickness/spacing: 0.5 mm/interleaved), axial T2*-weighted gradient echo images (TR/TE: 718/6 ms; matrix size: 256×256; slice thickness: 2 mm), and axial T1-weighted post-contrast FSE images (TR/TE: 720/11 ms; matrix size: 256×256; slice thickness/spacing: 1 mm/interleaved) were acquired. Post-contrast images were taken before and after the intravenous administration of an MRI contrast agent (MultiHance®, gadobenate dimeglumine; Bracco Diagnostics Inc, NJ USA; 0.21 ml/kg).

Visual Evoked Potentials (VEP) Recordings

EEG Electrode Implantation: A 9 mm rostrocaudal incision was made of the rat dorsal scalp (body weight 180–200 g) with surgical scissors and a scalpel. Then, 1-mm burr holes were drilled into the skull for two-electrode implantation. A stainless-steel skull screw (J.I. Morris, Southbridge, MA, USA) was implanted through the skull close to the visual cortex (6 mm posterior to bregma and 1 mm lateral to midline) as the signal electrode. A reference screw electrode was placed 2 mm anterior to bregma and 2 mm lateral to the midline. Dental cement (BASi, West Lafayette, IN, USA) was used to fix the screws. The skin incision was closed and 10 days were allowed for the animals to recover from the surgery before electroencephalography (EEG) recording.

EEG Recording and LED Stimulus Setup: EEG recording was performed with an 8 Channel Cyton Biosensing Board (OpenBCI, Brooklyn, NY, USA) with a custom firmware that allowed for a sampling rate of 500 Hz and for recording the stimulus timings. To prevent aliasing, samples were recorded at 16 kHz with digital filtering before resampling at 500 Hz, according to the specifications of the OpenBCI ADS1299. The OpenBCI board was also modified to interface with a laptop via a USB breakout board (Adafruit, NY, USA) and USB isolator (Adafruit, NY, USA). For EMI shielding, the box was placed in a Faraday Cage consisting of a cardboard box with aluminum foil and copper tape. The stimulus was provided by a Mini-Ganzfeld Stimulator consisting of a 3D-printed cone with three green LEDs (Linrose B4304H5–10, Plainview, NY, USA) embedded, and shielded with black electrical tape and copper mesh. A Raspberry Pi 2 Model B (RS Components Ltd., Corby, Northants, UK) was used to coordinate stimulus delivery. To gate the LED stimulus, the Raspberry Pi was connected to a breadboard (Twin Industries, San Ramon, CA) and a MOSFET (NTE, Bloomfield, NJ).

Combined FUS-EEG Setup: At least 10 days after electrode implantation, animals were anesthetized with ketamine/xylazine and were placed in a plastic stereotactic frame (Image Guided Therapy, Pessac, France) coupled to the FUS system, and immobilized with ear bars and a bite bar. Any remaining dorsal scalp fur in the sonication trajectory was removed by clipping and applying a chemical depilatory (Nair, amazon.com). A hair dryer was used for

20–30 s to remove moisture from around the electrodes. The signal and reference electrodes were coupled to the corresponding skull screw electrodes and the custom-made EEG system. A needle was inserted under the skin of the neck as the ground electrode. A digital multimeter was used to ensure that the electrode impedances were below 5. A monocular visual stimulus (Linrose B4304H5–10; 10ms flashes presented at 1 Hz) was applied contralateral to the sonicated hemisphere and the ipsilateral eye was covered with a plastic cone. A thin (< 1mm) ultrasound pad (Aquaflex®, Parker Laboratories, Inc., Fairfield, NJ, USA) and minimal ultrasound gel were used to couple the FUS transducer membrane and the skin of the head. Stereotactic coordinates for sonication are given in Table S2. The depth of sonication was controlled by adjusting the height of the coupling bag between the transducer face and the rat head. To account for skull attenuation, a 30% pressure insertion loss was assumed for this size and age of rats (O'Reilly et al., 2011). Prior to recording, animals were kept in a darkened room and allowed to adapt to darkness for at least 5 minutes.

Visual Evoked Potential (VEP) Recording: To ensure an adequate anesthesia plane was achieved to yield the appropriate signal-to-noise ratio for the experiment, VEP N1P1 amplitudes were monitored until the amplitude measured at least 60 μV over a 60 s epoch. Once this condition was achieved, 6 min VEP traces were acquired, with either focused ultrasound or nanoemulsion intravenous administration commencing at 3 min after the VEP recording started. At least 10 min passed between nanoemulsion administration and the next sonication.

PET Functional Imaging

Functional Imaging with [18F]-FDG: Dynamic PET Imaging was conducted on a Concorde Microsystems R4 MicroPET Scanner (Knoxville, TN). 5–7 rats (body weight 200–220g) were randomly assigned per condition. Rats were fasted overnight for 15–18 hours. Shortly before each scan, tail vein access was established via cannulation while the animal was anesthetized with 3% isoflurane. Dorsal scalp fur in the sonication trajectory was removed by clipping and applying a chemical depilatory (Nair, amazon.com). The midline and interaural line were drawn with a skin marker.

Then, the animals were taken off isoflurane and anesthetized with ketamine/xylazine. After the respiratory rate recovered to over 30 breaths per minute, the animals were placed in a plastic stereotactic frame (Image Guided Therapy, Pessac, France) coupled to the FUS system, and immobilized with ear bars and a bite bar. The transducer was aligned to 7 mm anterior to the interaural line (=2 mm caudal to bregma), 2 mm lateral of midline, 2 mm deep to skin for the cortical site and 6 mm anterior to interaural line (=3 mm caudal to bregma), 1.2 mm lateral of midline, and 5 mm deep to skin for the deep site. These coordinates are summarized in Table S2. The depth of sonication was controlled by adjusting the height of the coupling bag between the transducer face and the rat head. Ultrasound gel was used to couple the transducer to the skin. Then, the frame, including the FUS transducer, was placed within the scanner bore.

At the scan start, 2–2.2 mCi (in 150–500 μL) of [18 F]-Fluorodeoxyglucose (FDG) was administered through the tail vein catheter. Two minutes later, nanoemulsions were administered intravenously to a total encapsulated propofol dose of 1 mg/kg. Twelve minutes after administration of radiotracer (i.e., 10 minutes after nanoemulsion administration), FUS was applied while the animal was inside the PET scanner for four minutes for the given peak negative pressure, with a burst length of 50 ms and a burst repetition frequency of 1 Hz. To account for the skull and soft-tissue attenuation, attenuation coefficients were extrapolated from (O'Reilly et al., 2011). Scans were conducted for at least 30 minutes.

Images were then reconstructed with 0.85 mm (mediolateral) × 0.85 mm (dorsoventral) × 1.21 mm (anteroposterior) voxels, with 2-minute frames up to 8 minutes post radiotracer administration, after which 4-minute frames were used. Further analysis was done with the SimpleITK package in Python and the Fiji distribution of ImageJ (Schindelin et al., 2012).

In Vivo Characterization of the FUS Field: To determine the maximal extent of the sonication field for each target, and evaluate for any scattering, we used a blood-brain barrier (BBB) opening protocol similar to prior evaluations (McDannold et al., 2013). First, tail vein access was established via cannulation while the animal was anesthetized with 3% isoflurane. Dorsal scalp fur in the sonication trajectory was removed by clipping and applying a chemical depilatory (Nair, amazon.com). The midline and interaural line were drawn with a skin marker.

Then, animals were taken off isoflurane and anesthetized with ketamine/xylazine. After the respiratory rate recovered to over 30 breaths per minute, animals were placed in a plastic stereotactic frame (Image Guided Therapy, Pessac, France) coupled to the FUS system, and immobilized with ear bars and a bite bar. The transducer was aligned to either the cortical or deep site discussed in the PET section above. Ultrasound gel was used to couple the transducer with the skin. Definity® Microbubbles (20 μL/kg, Lantheus, N. Billerica, MA) were injected through the tail-vein cannula in a 1:10 dilution. Ten seconds after injection, FUS was applied for 5 minutes with an estimated peak *in situ* negative pressure of 0.4 MPa (~3x the estimated threshold intensity for this experiment), derated for the skull based on animal weight (O'Reilly et al., 2011), with a burst length of 10 ms and a burst repetition frequency of 1 Hz.

MRI evaluation was completed as discussed in the prior section. After sonication, axial T1-weighted fast spin-echo (FSE) images were taken (parameters: TR/TE: 720/11 ms; matrix size: 256/252; slice thickness: 1.5 mm) pre- and post-contrast intravenous administration. Post-contrast coronal T1-weighted FSE (TR/TE: 4800/68 ms; matrix size: 256×248; slice-thickness: 1.3 mm), axial T2*-weighted (same parameters as above), and axial T2-weighted (TR/TE: 5000/68 ms; matrix size: 256×248; slice thickness/s pacing: 1.3 mm) images were also acquired.

Calculation of heating induced by focused ultrasound protocols

To compute the estimated heating during each ultrasound pulse, we compute the intensity of ultrasound I as

$$I=\frac{P^2}{2Z}$$

where P is the peak negative pressure and Z is the acoustic impedance (ter Haar and Coussios, 2007). Additionally, we can derive from the ultrasound heat equation (Nyborg, 1988) the change in temperature per unit time $\frac{dT}{dt}$ as

$$\frac{dT}{dt}=\frac{2\alpha I}{\rho C}$$

where α is the tissue attenuation coefficient, ρ is the density of the material, and C is the specific heat. In the case of brain tissue, we set our constants as

$$Z=1.60\times10^6\frac{kg}{s\cdot m^2}$$
$$\rho=1.03\frac{g}{cm^3}$$
$$\alpha=0.44\frac{dB}{cm}$$
$$C=3630\frac{J}{kg\cdot{}^\circ C}$$

as taken or derived from published values for each (Azhari, 2010; Hasgall et al., 2015). Computing with these constants give an estimated temperature rate of rise during sonication at P=1.2 and 1.8 MPa peak negative pressure of 1 °C/s and 2 °C/s respectively. Given that we sonicate with pulses that are maximally 0.1 s at 1.2 MPa and 0.05 s at 1.8 MPa, we expect temperature rises of up to 0.1 °C per pulse in either condition.

Quantification and Statistical Analysis

All data was analyzed and plotted using custom code written in Python.

EEG Recordings

EEG Preprocessing: Raw EEG traces were digitally filtered with a 4th order bandpass Butterworth filter with cutoff frequencies of 1–100 Hz. Notch filtering for 60 Hz noise and its higher harmonics consisted of 2nd order digital Chebyshev filters with cutoff frequencies of 58–62 Hz, 118–122 Hz, 178–182 Hz, and 238–242 Hz. VEP traces were computed by averaging over all presented VEP stimuli over a 60 second period with a Gaussian kernel with a standard deviation of 20 seconds. The N1P1 amplitude for averaged VEP traces was quantified by finding the first local minimum 40 ms after stimulus onset, then finding the next local maximum, and then taking the difference. Traces consisting of N1P1 amplitudes that swung between adjacent presentations of more than 30 μV in either direction were excluded because they were indicative of VEP traces that were too unstable to quantify due

to spiking electrical artifacts. All traces were then normalized by dividing by the averaged N1P1 amplitudes over the period from 0 to 120 seconds.

Within a single experiment, we have multiple traces for which we applied sonication after injection of nanoparticles. First, we average over all of the traces within that single experiment to generate a single averaged trace per experiment. Then we average over all of these averaged traces for all experiments with a given condition. We define N in this case to be the number of recording sessions conducted.

Electrophysiologic Effect Quantification: For quantification of effect size and recovery time, we use the piecewise model

$$VEP\left(t; k_{on}, k_{off}\right) = \begin{cases} 1, & t < 180 \\ 1 - k_{on}(t - 180), & 180 \leq t < 240 \\ 1 - 60k_{on}e^{-koff(t-240)}, & 240 \leq t \end{cases}$$

where t represents the experiment time (in minutes), k_{on} represents the rate of suppression by propofol, and k_{off} represents the rate of recovery. To fit against our experimental data, we first sample the model at the same time points as from our quantification of the N1P1 amplitude, then digitally apply a Gaussian Kernel to our model over a period of 60 seconds with a standard deviation for 20 seconds to mimic the averaging of N1P1 amplitudes from our analysis (Fig. S2A). We then fit our two parameters by least-squares regression with the Trust Region Reflective variant of the Levenberg-Marquardt method (Fig. S2B). We report root mean square errors (RMSE) in Table S1. With our fit parameters, we can now define our effect size and recovery half-life time as

$$\text{Effect Size} = \text{N1P1 Difference} = 1 - VEP(240)$$

$$\text{Recovery Time} = \frac{\ln(2)}{k_{off}}$$

To estimate the errors of our experiments, we utilize a boot-strap technique. Let N be the number of experiments for a given condition. For 500 times, we sample N experiments, with replacement, and generate the trace using the double averaging method described above. Then, we estimate our parameters. We take the standard deviation of our trials and divide by $\sqrt{N}$ to compute the SEM of the estimated parameters.

PET Imaging

Quantification of PET Effect Size: To determine the effect size, we first identified the midline and the interaural line on the image taken from 12–16 minutes (i.e., during sonication). To define the sonication region of interest, we used the same landmarks as when physically positioning the transducer (using the cerebellum/cerebrum border as the

interaural line) and measured our coordinates as given in Table S2. We then determined the voxel with the minimal FDG uptake (under an assumption of detecting a decrease, as we are uncaging an anesthetic) in a 3 × 3 mm region centered on that measured target and used that to define the center of the measured effect. This procedure was completed exactly in the same fashion for all groups, including for blank nanoparticle sonication.

We normalized by using the same quantification method on the contralateral side (4 mm lateral to sonication for the cortical site, 3 mm for the deep site). We then report the ratio of the sonication area to the contralateral site. For our time activity curve (TAC) analysis, we carry out the same quantification method for each frame.

Effect Full-Width Half-Max (FWHM) Quantification: We quantify the effect FWHM from the cortical sonication experiments. First, we interpolated our images via cubic interpolation. Then, the ROI from the quantification of the effect size was identified on the sonication image. 1-D curves were generated to identify the local minima and its adjacent local maxima along the right-left and ventral-dorsal axis. For the right-left axis, FWHM was defined as the total distance for FDG avidity to recover to half of the distance between the local minima at the focus and its local maxima. For the ventral-dorsal axis, because our focus site was cortical, we instead defined the half-max distance as the distance over which FDG avidity reached half of its maximum value moving ventrally beyond the focus, and computed the FWHM by dividing this distance by 60%, as 60% of the distance covered by the FWHM is beyond the focus distal to the transducer according to simulations and hydrophone recordings of the transducer sonication field.

Generation of Statistical Parametric Maps: First, all images were manually cropped to include only the brain to ease coregistration. Images were then coregistered against one of the scans taken with sonication of blank nanoemulsions for each site. Coregistration was performed in Simple ITK, with first a rigid-body transformation and then an affine optimization. Interpolation was performed with a Hamming windowed sinc function. Similarity measures were computed by thresholding the images against the median and then taking the root mean square error. For the affine optimization, the Nelder-Mead method was used, with a function convergence tolerance of 10^{-6}. After coregistration, the cerebellum was identified for the fixed blank image used for coregistration, and this ROI was used for all coregistered images for normalization as discussed below.

To compute statistical parametric maps, for each scan within the condition we selected the sonication frame and the frame taken from 24–28 min (i.e. the final frame taken). We subtracted the final frame from the sonication frame and then divided by the mean value from the cerebellum ROI derived for normalization. We then repeated this process across all scans for the same condition. Then for each voxel, we computed the z-score by taking the average normalized difference and then dividing by the standard error across all experiments for that specific voxel, with N defined as the number of imaging sessions conducted under that specific condition. We thresholded our images by the voxel-wise Bonferonni corrected alpha value of 0.05 (i.e., $p \leq 10^{-5}$, $Z \leq -4.25$).

Supplementary Material

Refer to Web version on PubMed Central for supplementary material.

Acknowledgments:

We would like to thank W.T. Newsome, K.B. Pauly, J. Kubanek, F.T. Chin, M.B. MacIver, and the whole Airan Lab for helpful discussions and use of equipment. We would also like to thank H. Lorach, F. Habte, A. Pascal-Tenorio, and Z. Huang, for assistance in training and implementation of the varied experimental protocols. We would like to thank A. Thomas for assistance in figure preparation. This work was funded with grant support from the National Institutes of Health (BRAIN Initiative RF1 MH114252), the Stanford Center for Cancer Nanotechnology Excellence (NIH U54 CA199075), the Foundation of the American Society for Neuroradiology, the Wallace H. Coulter Foundation, the Dana Foundation, and W.T. Newsome and the Stanford Neurosciences Institute. Fellowship funding was provided by the Stanford Medical Scientist Training Program (MSTP; NIH T32 GM007365; JBW) and the Stanford Cancer Imaging Training program (SCIT; NIH T32 CA009695; MRA).

References:

Airan R (2017). Neuromodulation with nanoparticles. Science (New York, N.Y.) 357, 465.

Airan RD, Meyer RA, Ellens NPK, Rhodes KR, Farahani K, Pomper MG, Kadam SD, and Green JJ (2017). Noninvasive Targeted Transcranial Neuromodulation via Focused Ultrasound Gated Drug Release from Nanoemulsions. Nano Letters 17, 652–659. [PubMed: 28094959]

Allan C, Kalu U-G, Sexton CE, Ebmeier KP, Kennedy S, Giacobbe P, Allan C, Herrmann L, Ebmeier K, Slotema C, et al. (2012). Transcranial stimulation in depression. The British Journal of Psychiatry : The Journal of Mental Science 200, 10–11. [PubMed: 22215863]

Azhari H (2010). Basics of biomedical ultrasound for engineers (Wiley).

Bichot NP, Heard MT, and Desimone R (2011). Stimulation of the nucleus accumbens as behavioral reward in awake behaving monkeys. Journal of Neuroscience Methods 199, 265–272. [PubMed: 21704383]

Bosch-Bouju C, Hyland BI, and Parr-Brownlie LC (2013). Motor thalamus integration of cortical, cerebellar and basal ganglia information: implications for normal and parkinsonian conditions. Frontiers in Computational Neuroscience 7, 163. [PubMed: 24273509]

Brown EN, Purdon PL, and Van Dort CJ (2011). General anesthesia and altered states of arousal: a systems neuroscience analysis. Annual Review of Neuroscience 34, 601–628.

Casella DP, Dudley AG, Clayton DB, Pope JC, Tanaka ST, Thomas J, Adams MC, Brock JW, and Caskey CF (2017). Modulation of the rat micturition reflex with transcutaneous ultrasound. Neurourology and Urodynamics 36, 1996–2002. [PubMed: 28346718]

Chaplin V, Phipps MA, and Caskey CF (2018). A random phased-array for MR-guided transcranial ultrasound neuromodulation in non-human primates. Physics in Medicine and Biology

Chen Y, and Liu L (2012). Modern methods for delivery of drugs across the blood–brain barrier. Advanced Drug Delivery Reviews 64, 640–665. [PubMed: 22154620]

Chen R, Romero G, Christiansen MG, Mohr A, and Anikeeva P (2015). Wireless magnetothermal deep brain stimulation. Science (New York, N.Y.) 347, 1477–1480.

Chesney MA, Perouansky M, and Pearce RA (2003). Differential uptake of volatile agents into brain tissue in vitro. Anesthesiology 99, 122–130. [PubMed: 12826851]

Cinelli AR, Ferreyra-Moyano H, and Barragan E (1987). Reciprocal functional connections of the olfactory bulbs and other olfactory related areas with the prefrontal cortex. Brain Research Bulletin 19, 651–661. [PubMed: 3440217]

Courtiol E, and Wilson DA (2014). Thalamic olfaction: characterizing odor processing in the mediodorsal thalamus of the rat. Journal of Neurophysiology 111, 1274–1285. [PubMed: 24353302]

Deffieux T, Younan Y, Wattiez N, Tanter M, Pouget P, and Aubry J-F (2013). Low-Intensity Focused Ultrasound Modulates Monkey Visuomotor Behavior. Current Biology 23, 2430–2433. [PubMed: 24239121]

Ellender TJ, Harwood J, Kosillo P, Capogna M, and Bolam JP (2013). Heterogeneous properties of central lateral and parafascicular thalamic synapses in the striatum. Journal of Physiology 591, 257–272. [PubMed: 23109111]

Fabiilli ML, Haworth KJ, Sebastian IE, Kripfgans OD, Carson PL, and Fowlkes JB (2010). Delivery of Chlorambucil Using an Acoustically-Triggered Perfluoropentane Emulsion. Ultrasound in Medicine & Biology 36, 1364–1375. [PubMed: 20691925]

Farzan F, Vernet M, Shafi MMD, Rotenberg A, Daskalakis ZJ, and Pascual-Leone A (2016). Characterizing and Modulating Brain Circuitry through Transcranial Magnetic Stimulation Combined with Electroencephalography. Frontiers in Neural Circuits 10, 73. [PubMed: 27713691]

Ghanouni P, Pauly KB, Elias WJ, Henderson J, Sheehan J, Monteith S, and Wintermark M (2015). Transcranial MRI-Guided Focused Ultrasound: A Review of the Technologic and Neurologic Applications. AJR. American Journal of Roentgenology 205, 150–159. [PubMed: 26102394]

Gredell JA, Turnquist PA, Maciver MB, and Pearce RA (2004). Determination of diffusion and partition coefficients of propofol in rat brain tissue: implications for studies of drug action in vitro. British Journal of Anaesthesia 93, 810–817. [PubMed: 15377586]

Van Groen T, and Wyss JM (1990). Extrinsic projections from area CA1 of the rat hippocampus: Olfactory, cortical, subcortical, and bilateral hippocampal formation projections. The Journal of Comparative Neurology 302, 515–528. [PubMed: 1702115]

Grossman N, Bono D, Dedic N, Kodandaramaiah SB, Rudenko A, Suk H-J, Cassara AM, Neufeld E, Kuster N, Tsai L-H, et al. (2017). Noninvasive Deep Brain Stimulation via Temporally Interfering Electric Fields. Cell 169, 1029–1041.e16. [PubMed: 28575667]

Guo H, Hamilton M, Offutt SJ, Gloeckner CD, Li T, Kim Y, Legon W, Alford JK, and Lim HH (2018). Ultrasound Produces Extensive Brain Activation via a Cochlear Pathway. Neuron

ter Haar G, and Coussios C (2007). High intensity focused ultrasound: Physical principles and devices. International Journal of Hyperthermia 23, 89–104. [PubMed: 17578335]

Hasgall P, Di Gennaro F, Baumgartner C, Neufeld E, Gosselin M, Payne D, Klingenböck A, and Kuster N (2015). IT'IS Datab ase for Thermal and Electromagnetic Parameters of Biological Tissues Www.Itis.Ethz.Ch/DatabaseVersion2.6.

Heckers S, Geula C, and Mesulam M-M (1992). Cholinergic innervation of the human thalamus: Dual origin and differential nuclear distribution. The Journal of Comparative Neurology 325, 68–82. [PubMed: 1282919]

Hess US, Lynch G, and Gall CM (1995). Changes in c-fos mRNA expression in rat brain during odor discrimination learning: differential involvement of hippocampal subfields CA1 and CA3. The Journal of Neuroscience : The Official Journal of the Society for Neuroscience 15, 4786–4795. [PubMed: 7623110]

Hudetz AG (1997). Blood Flow in the Cerebral Capillary Network: A Review Emphasizing Observations with Intravital Microscopy. Microcirculation 4, 233–252. [PubMed: 9219216]

Hynynen K, and Jolesz FA (1998). Demonstration of potential noninvasive ultrasound brain therapy through an intact skull. Ultrasound in Medicine & Biology 24, 275–283. [PubMed: 9550186]

Ibsen S, Tong A, Schutt C, Esener S, and Chalasani SH (2015). Sonogenetics is a non-invasive approach to activating neurons in Caenorhabditis elegans. Nature Communications 6, 8264.

Jespersen SN, and Østergaard L (2012). The rol es of cerebral blood flow, capillary transit time heterogeneity, and oxygen tension in brain oxygenation and metabolism. Journal of Cerebral Blood Flow and Metabolism 32, 264–277. [PubMed: 22044867]

Jorgenson LA, Newsome WT, Anderson DJ, Bargmann CI, Brown EN, Deisseroth K, Donoghue JP, Hudson KL, Ling GSF, MacLeish PR, et al. (2015). The BRAIN Initiative: developing technology to catalyse neuroscience discovery. Philosophical Transactions of the Royal Society of London. Series B, Biological Sciences 370, 214–222.

King RL, Brown JR, Newsome WT, and Pauly KB (2013). Effective parameters for ultrasound-induced in vivo neurostimulation. Ultrasound in Medicine & Biology 39, 312–331. [PubMed: 23219040]

Lee RMKW (1995). Morphology of cerebral arteries. Pharmacology & Therapeutics 66, 149–173. [PubMed: 7630927]

Lee H-M, Giguere PM, and Roth BL (2014). DREADDs: novel tools for drug discovery and development. Drug Discovery Today 19, 469–473. [PubMed: 24184433]

Lee JY, Carugo D, Crake C, Owen J, de Saint Victor M, Seth A, Coussios C, and Stride E (2015). Nanoparticle-Loaded Protein-Polymer Nanodroplets for Improved Stability and Conversion Efficiency in Ultrasound Imaging and Drug Delivery. Advanced Materials (Deerfield Beach, Fla.) 27, 5484–5492.

Lee W, Croce P, Margolin RW, Cammalleri A, Yoon K, and Yoo S-S (2018). Transcranial focused ultrasound stimulation of motor cortical areas in freely-moving awake rats. BMC Neuroscience 19, 57. [PubMed: 30231861]

Legon W, Sato TF, Opitz A, Mueller J, Barbour A, Williams A, and Tyler WJ (2014). Transcranial focused ultrasound modulates the activity of primary somatosensory cortex in humans. Nature Neuroscience 17, 322–329. [PubMed: 24413698]

Leuchter B, Pedley TA, Lisanby SH, Mayberg HS, and Schiff ND (2012). Brain stimulation in neurology and psychiatry: perspectives on an evolving field. Annals of the New York Academy of Sciences 1265, vii–x. [PubMed: 22882334]

Lipsman N, Mainprize TG, Schwartz ML, Hynynen K, and Lozano AM (2014). Intracranial Applications of Magnetic Resonance-guided Focused Ultrasound. Neurotherapeutics 11, 593–605. [PubMed: 24850310]

Lipsman N, Meng Y, Bethune AJ, Huang Y, Lam B, Masellis M, Herrmann N, Heyn C, Aubert I, Boutet A, et al. (2018). Blood–br ain barrier opening in Alzheimer's disease using MR-guided focused ultrasound. Nature Communications 9, 2336.

Liu J, Lee HJ, Weitz AJ, Fang Z, Lin P, Choy M, Fisher R, Pinskiy V, Tolpygo A, Mitra P, et al. (2015). Frequency-selective control of cortical and subcortical networks by central thalamus. ELife 4, e09215. [PubMed: 26652162]

Makadia HK, and Siegel SJ (2011). Poly Lactic-co-Glycolic Acid (PLGA) as Biodegradable Controlled Drug Delivery Carrier. Polymers 3, 1377–1397. [PubMed: 22577513]

Mayberg HS, Lozano AM, Voon V, McNeely HE, Seminowicz D, Hamani C, Schwalb JM, and Kennedy SH (2005). Deep Brain Stimulation for Treatment-Resistant Depression. Neuron 45, 651–660. [PubMed: 15748841]

McCarthy MM, and Kopell N (2012). The Effect of Propofol Anesthesia on Rebound Spiking. SIAM Journal on Applied Dynamical Systems 11, 1674–1697.

McDannold N, Zhang Y-Z, Power C, Jolesz F, and Vykhodtseva N (2013). Nonthermal ablation with microbubble-enhanced focused ultrasound close to the optic tract without affecting nerve function. Journal of Neurosurgery 119, 1208–1220. [PubMed: 24010975]

McDannold N, Zhang Y, Power C, Arvanitis CD, Vykhodtseva N, and Livingstone M (2015). Targeted, noninvasive blockade of cortical neuronal activity. Scientific Reports 5, 16253. [PubMed: 26542745]

Nortmann N, Rekauzke S, Azimi Z, Onat S, KÃ¶nig P, and Jancke D (2015). Visual homeostatic processing in V1: when probability meets dynamics. Frontiers in Systems Neuroscience 9, 6. [PubMed: 25691861]

Nyborg WL (1988). Solutions of the bio-heat transfer equation. Phys. Med. Biol 33, 785. [PubMed: 3212041]

O'Reilly MA, Huang Y, and Hynynen K (2010). The impact of standing wave effects on transcranial focused ultrasound disruption of the blood–brain barrier in a rat model. Physics in Medicine and Biology 55, 5251–5267. [PubMed: 20720286]

O'Reilly MA, Muller A, and Hynynen K (2011). Ultrasound insertion loss of rat parietal bone appears to be proportional to animal mass at submegahertz frequencies. Ultrasound in Medicine & Biology 37, 1930–1937. [PubMed: 21925788]

Paxinos G, and Watson C (2013). The Rat Brain in Stereotaxic Coordinates : Hard Cover Edition. (Elsevier Science).

Rapoport N (2012). Phase-shift, stimuli-responsive perfluorocarbon nanodroplets for drug delivery to cancer. Wiley Interdisciplinary Reviews. Nanomedicine and Nanobiotechnology 4, 492–510. [PubMed: 22730185]

Rapoport N (2016). Drug-Loaded Perfluorocarbon Nanodroplets for Ultrasound-Mediated Drug Delivery. Advances in Experimental Medicine and Biology 880, 221–241. [PubMed: 26486341]

Robbin ML, and Eisenfeld AJ (1998). Perflenapent emulsion: a US contrast agent for diagnostic radiology--multicenter, double-blind comparison with a placebo. EchoGen Contrast Ultrasound Study Group. Radiology 207, 717–722. [PubMed: 9609895]

Rubelowski JM, Menge M, Distler C, Rothermel M, and Hoffmann K-P (2013). Connections of the superior colliculus to shoulder muscles of the rat: a dual tracing study. Frontiers in Neuroanatomy 7, 17. [PubMed: 23760726]

Sanchez-Vives MV, Nowak LG, and McCormick D a (2000). Cellular mechanisms of long-lasting adaptation in visual cortical neurons in vitro. The Journal of Neuroscience : The Official Journal of the Society for Neuroscience 20, 4286–4299. [PubMed: 10818164]

Sato T, Shapiro MG, and Tsao DY (2018). Ultrasonic Neuromodulation Causes Widespread Cortical Activation via an Indirect Auditory Mechanism. Neuron

Schindelin J, Arganda-Carreras I, Frise E, Kaynig V, Longair M, Pietzsch T, Preibisch S, Rueden C, Saalfeld S, Schmid B, et al. (2012). Fiji: an open-source platform for biological-image analysis. Nature Methods 9, 676–682. [PubMed: 22743772]

Sheeran PS, and Dayton PA (2012). Phase-Change Contrast Agents for Imaging and Therapy. Current Pharmaceutical Design 18, 2152–2165. [PubMed: 22352770]

Sheeran PS, Matsuura N, Borden MA, Williams R, Matsunaga TO, Burns PN, and Dayton PA (2016). Methods of Generating Sub-Micron Phase-Shift Perfluorocarbon Droplets for Applications in Medical Ultrasonography. IEEE Transactions on Ultrasonics, Ferroelectrics, and Frequency Control 1–1.

Sieu L-A, Bergel A, Tiran E, Deffieux T, Pernot M, Gennisson J-L, Tanter M, and Cohen I (2015). EEG and functional ultrasound imaging in mobile rats. Nature Methods 12, 831–834. [PubMed: 26237228]

Spruston N (2008). Pyramidal neurons: dendritic structure and synaptic integration. Nature Reviews Neuroscience 9, 206–221. [PubMed: 18270515]

Szablowski JO, Lue B, Lee-Gosselin A, Malounda D, and Shapiro Mi.G. (2018). Acoustically Targeted Chemogenetics for Noninvasive Control of Neural Circuits. BioRxiv 241406.

Tasbihgou SR, Netkova M, Kalmar AF, Doorduin J, Struys MMRF, Schoemaker RG, and Absalom AR (2018). Brain changes due to hypoxia during light anaesthesia can be prevented by deepening anaesthesia; a study in rats. PLOS ONE 13, e0193062. [PubMed: 29451906]

Tiran E, Ferrier J, Deffieux T, Gennisson J-L, Pezet S, Lenkei Z, and Tanter M (2017). Transcranial Functional Ultrasound Imaging in Freely Moving Awake Mice and Anesthetized Young Rats without Contrast Agent. Ultrasound in Medicine & Biology 43, 1679–1689. [PubMed: 28476311]

Tyler WJ, Lani SW, and Hwang GM (2018). Ultrasonic modulation of neural circuit activity. Current Opinion in Neurobiology 50, 222–231. [PubMed: 29674264]

Upton RN (2007). Cerebral uptake of drugs in humans. Clinical and Experimental Pharmacology & Physiology 34, 695–701. [PubMed: 17600543]

Upton RN, and Ludbrook GL (1997). A physiological model of induction of anaesthesia with propofol in sheep. 1. Structure and estimation of variables. British Journal of Anaesthesia 79, 497–504. [PubMed: 9389270]

Urban A, Dussaux C, Martel G, Brunner C, Mace E, and Montaldo G (2015). Real-time imaging of brain activity in freely moving rats using functional ultrasound. Nature Methods 12, 873–878. [PubMed: 26192084]

Vöröslakos M, Takeuchi Y, Brinyiczki K, Zombo ri T, Oliva A, Fernández-Ruiz A, Kozák G, Kincses ZT, Iványi B, Buzsáki Get., al. (2018). Direct effects of transcranial electric stimulation on brain circuits in rats and humans. Nature Communications 9, 483.

Xiong B, Li A, Lou Y, Chen S, Long B, Peng J, Yang Z, Xu T, Yang X, Li X, et al. (2017). Precise Cerebral Vascular Atlas in Stereotaxic Coordinates of Whole Mouse Brain. Frontiers in Neuroanatomy 11, 128. [PubMed: 29311856]

Yang Y, Cui Y, Sang K, Dong Y, Ni Z, Ma S, and Hu H (2018). Ketamine blocks bursting in the lateral habenula to rapidly relieve depression. Nature 554, 317–322. [PubMed: 29446381]

Ye PP, Brown JR, and Pauly KB (2016). Frequency Dependence of Ultrasound Neurostimulation in the Mouse Brain. Ultrasound in Medicine & Biology 42, 1512–1530. [PubMed: 27090861]

Younan Y, Deffieux T, Larrat B, Fink M, Tanter M, and Aubry J-F (2013). Influence of the pressure field distribution in transcranial ultrasonic neurostimulation. Medical Physics 40, 082902. [PubMed: 23927357]

Zhang F, Gradinaru V, Adamantidis AR, Durand R, Airan RD, de Lecea L, and Deisseroth K (2010). Optogenetic interrogation of neural circuits: technology for probing mammalian brain structures. Nature Protocols 5, 439–456. [PubMed: 20203662]

Zhong Q, Yoon BC, Aryal MR, Wang JB, and Airan RD (2018). Polymeric Perfluorocarbon Nanodroplets for Noninvasive Focal Uncaging of Hydrophobic Drugs in vivo with Focused Ultrasound. In Proceedings of the Controlled Release Society, (New York, NY), p. 299.

Highlights

- Ultrasound-sensitive nanoparticles enable localized drug delivery to the brain
- Ultrasonic drug uncaging allows noninvasive and precise control of brain activity
- Drug effects are limited to the ultrasound focus and by the kinetics of the drug
- Uncaging and neuroimaging together causatively maps whole-brain functional networks

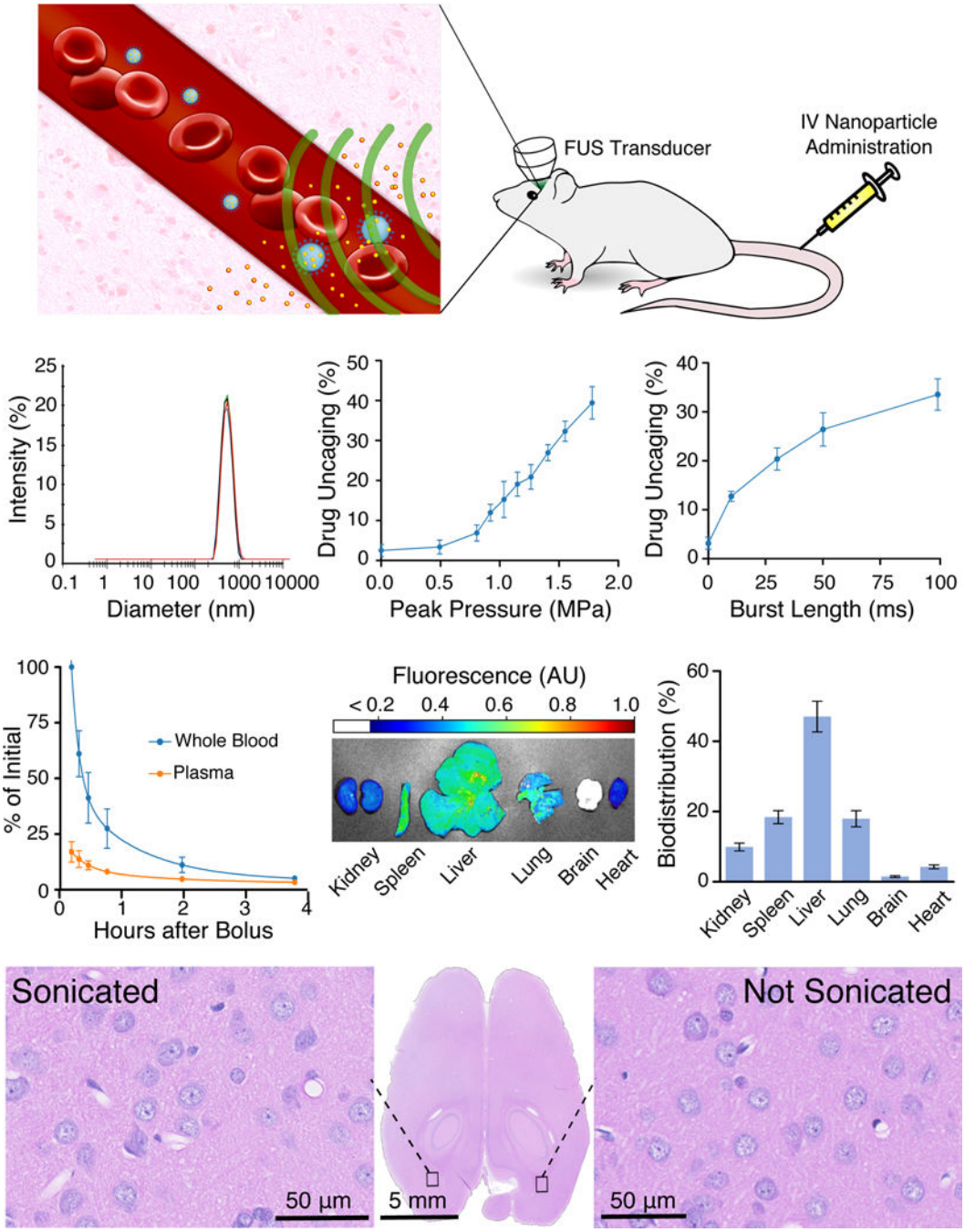

Fig. 1: Nanoparticles for ultrasonic drug uncaging are effective and well-tolerated.

(**A**) Schematic of nanoparticle use. Intravenously administered nanoparticles (blue) distribute in the blood volume. When focused ultrasound (FUS; green) is applied to a parenchymal target, drug (yellow) is uncaged from the nanoparticles into the blood, and then the drug diffuses into the brain across the blood-brain barrier. (**B**) Typical nanoparticle dynamic light scattering results show a monodisperse peak of nanoscale material with Z-averaged diameter 397.3 ± 10.0 nm, polydispersity index 0.068 ± 0.023, zeta potential −26.7 ± 0.6 mV. (**C**) Drug uncaging efficacy *in vitro* with 650 kHz focused sonication, while

varying *in situ* pressure (left; with 60 × 50 ms burst length at 1 Hz burst frequency) or burst length (right; with 1.2 MPa peak *in situ* pressure) applied to an aqueous suspension of propofol-loaded nanoparticles quantified by the amount of uncaged drug that partitions to an organic solvent as a fraction of the total loaded drug (N=3, mean +/− S.E.M.). (**D**) Particle clearance kinetics in whole blood and plasma following intravenous bolus administration of 1 mg/kg of propofol encapsulated in nanoparticles doped with an infrared fluorescent dye. Curves represent a double-exponential model fit to the data (N=3, mean +/− S.E.M.). (**E**) Nanoparticle biodistribution in a single animal (left) and quantified (right; N=3, mean +/− S.E.M.) in end organs 24 h after intravenous bolus administration of propofol-loaded nanoparticles doped with an infrared fluorescent dye, presented as the percent of fluorescence seen across the six harvested organs. (**F**) Representative hematoxylin and eosin-stained transverse section of the brain (center) of a rat administered propofol-loaded nanoparticles intravenously and exposed to focused sonication (60 × 100 ms bursts with 1 Hz burst frequency at 1.8 MPa) directed to the occipital cortex, with 40x views of the sonication target (left) and the contralateral non-sonicated brain (right).

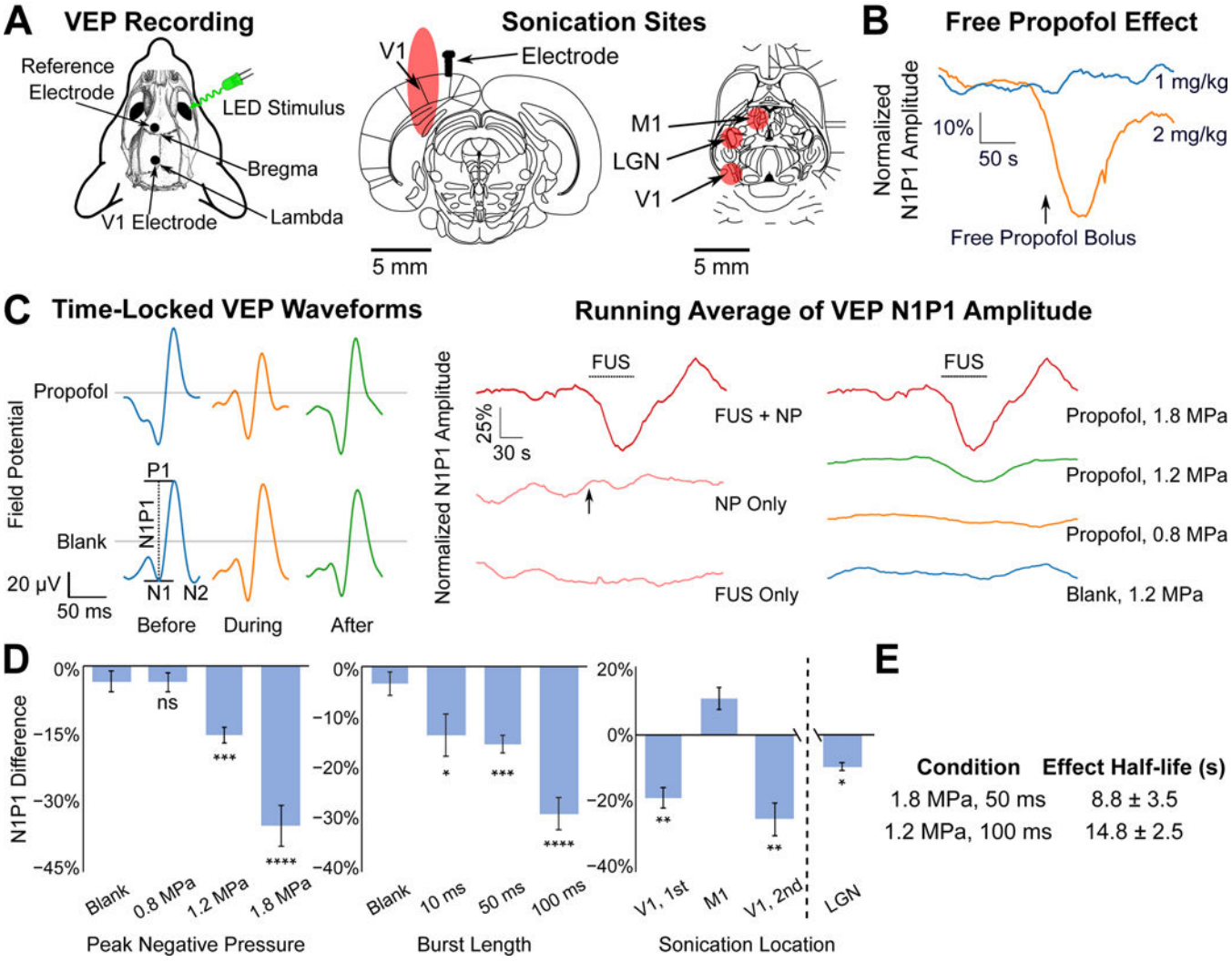

Fig. 2: Dose-response relationship and temporal kinetics of ultrasonic propofol uncaging, revealed by visual evoked potentials (VEPs).

(**A**) Schematic of recording electrode and light stimulus configuration (*left*) and sonication sites (*right*) represented by the expected full-width half-maximum (FWHM) of the sonication targets overlaid onto atlas slices (Paxinos and Watson, 2013) *middle*: −6.5 mm caudal to bregma, *right*: −5.1 mm ventral to bregma. V1: primary visual cortex, M1: primary motor cortex, LGN: lateral geniculate nucleus. (**B**) Running average (N=3 animals each) of the VEP N1P1 amplitude over time during a flashing light stimulus (10 ms monocular light stimulus at 1 Hz), normalized by the 60 seconds of stimulus presentation prior to bolus administration. Intravenous free propofol administration shows no effect with a 1 mg/kg bolus (blue) of free propofol, and a pronounced effect only with 2 mg/kg (orange). In all nanoparticle experiments, 1 mg/kg of encapsulated propofol was given in a bolus. (**C**) *Left*: Time-locked VEP waveforms (10 ms monocular light stimulus at 1 Hz), averaged over 60 s from an individual representative session before, during, or after sonication (60 × 50 ms bursts, 1 Hz burst frequency at 1.2 MPa est. peak *in situ* pressure) applied to V1 contralateral from the light stimulus, following intravenous administration of propofol-loaded (*top*) or

blank (*bottom*) nanoparticles. Scheme of N1P1 amplitude measurement indicated on the bottom left waveform. *Middle*: Running average (N=5 animals) of the VEP N1P1 amplitude over time for presentations of focused ultrasound (FUS) only (*bottom*; 60 × 50 ms bursts, 1 Hz burst frequency at 1.8 MPa est. peak *in situ* pressure), followed by nanoparticle (NP) administration (*middle*; arrow indicates start of bolus administration), and then focused ultrasound with nanoparticles in circulation (FUS + NP, *top*) during the indicated time period (dashed bar). Time traces are normalized by the 60 seconds prior to intervention (i.e., FUS for the "F US + NP" and "FUS Only" conditions or bolus administration for the NP Only condition) *Right*: Running average (N=5–9 animals) of VEP N1P1 amplitude following sonication (60 × 50 ms bursts, 1 Hz burst frequency) applied to V1 With the indicated peak *in situ* pressure, normalized by the 60 seconds prior to FUS administration. 1.8 MPa trace repeated from the middle panel. Dashed bar: sonication time. (**D**) Quantification of the difference in N1P1 amplitude seen between the beginning and end of sonication (60 bursts at 1 Hz burst frequency) while varying the peak *in situ* pressure (*left*; 50 ms bursts) or burst length (*middle*; 1.2 MPa pressure); and for two separate experiments (*right*) first while moving the sonication (1.2 MPa, 60 × 50 ms bursts, 1 Hz burst frequency) between V1 and M1 successively in the same animal (statistical comparison to M1 sonication), or separately sonicating LGN. Presented are mean +/− S.E.M. for groups of N=4–9. *: $p<0.05$, **: $p<0.01$, ***: $p<0.001$, by two-tailed t-tests, comparing to blank nanoparticle sonication unless otherwise noted. Process for computing the difference in N1P1 amplitude is described in STAR Methods. (**E**) Effect half-life indicated by a model (see Fig. S2, STAR Methods) fitted to the N1P1 time traces for the indicated condition.

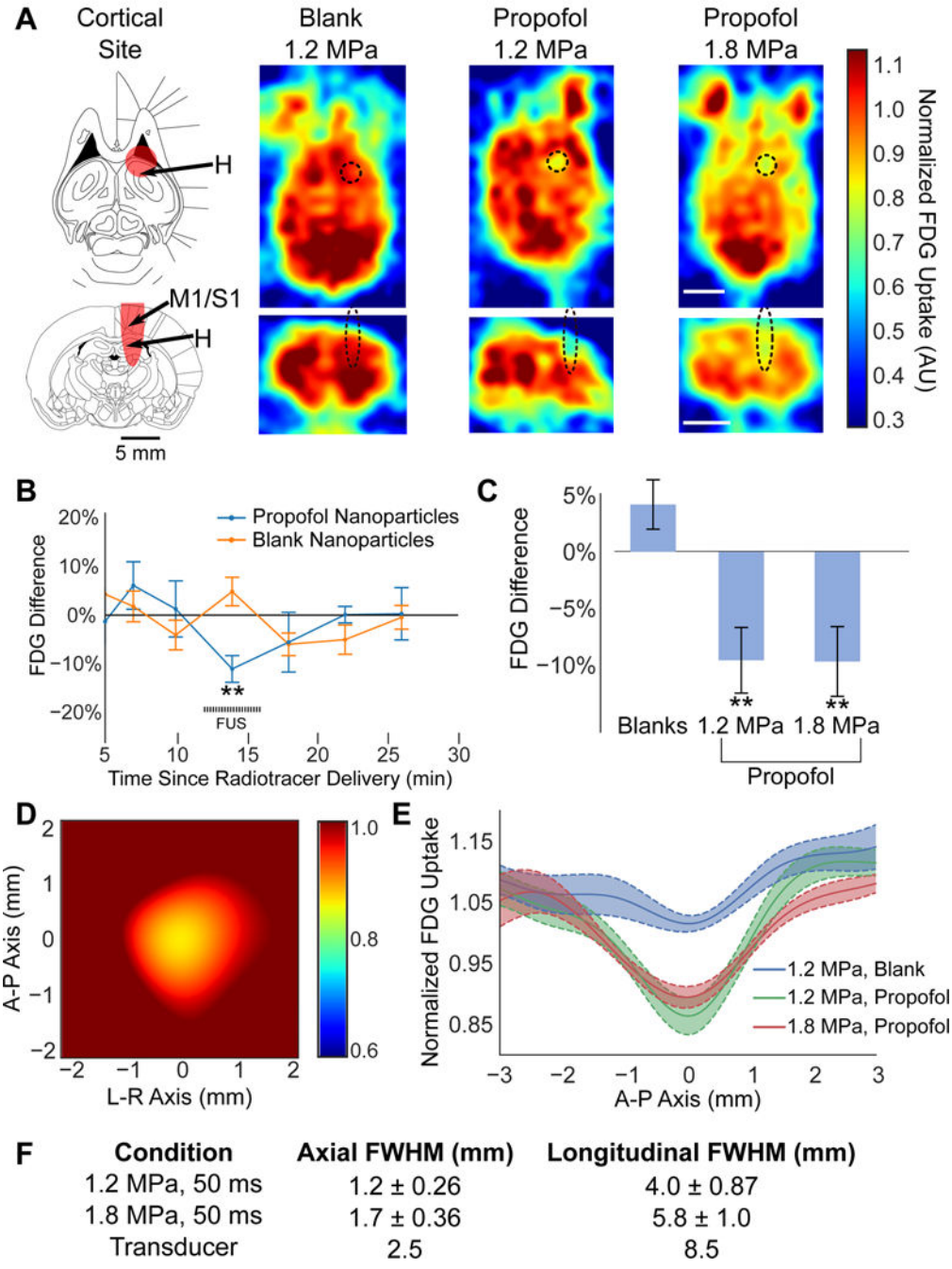

F

Condition	Axial FWHM (mm)	Longitudinal FWHM (mm)
1.2 MPa, 50 ms	1.2 ± 0.26	4.0 ± 0.87
1.8 MPa, 50 ms	1.7 ± 0.36	5.8 ± 1.0
Transducer	2.5	8.5

Figure 3: Spatial profile of ultrasonic drug uncaging quantified by PET imaging.

(**A**) *Left*: Full-width half-maximum (FWHM) of the cortical sonication target (red) indicated on atlas sections (Paxinos and Watson, 2013) *top*: −6.9 mm ventral to bregma, *bottom*: −2 mm caudal to bregma. H: Hippocampus, M1: Primary motor cortex, S1: Primary somatosensory cortex. *Right*: Transverse (*top*) and axial (*bottom*) PET images obtained during sonication (60 × 50 ms bursts at 1 Hz burst frequency; black dashed ellipse: expected sonication FWHM) at the indicated peak *in situ* pressure, following blank or propofol-loaded nanoparticle administration. Color bar represents FDG uptake, normalized against

the average FDG uptake in the contralateral hemisphere. Note that the anterior paired structures outside the brain are the Harderian glands. Scale bar: 5 mm. (**B**) Difference of the minimum FDG avidity across time for the voxels within the sonication FWHM averaged across animals receiving blank (orange) or propofol-loaded (blue) nanoparticles at 2 min following radiotracer administration. FDG avidity values are normalized against the contralateral field to account for different temporal features of FDG uptake in different animals, due to different body weights, blood glucose level, and general anesthesia level (Fig. S3B). (**C**) Quantification of FDG uptake during sonication for voxels in the sonication field minus the contralateral non-sonicated field following blank or propofol-loaded nanoparticle administration. (**D)** Locally registered, interpolated, and averaged image of FDG uptake at the sonication site for 1.2 MPa sonication with propofol-loaded nanoparticles, normalized by the contralateral field. A-P: anterior-posterior; L-R: left-right. (**E)** FDG uptake across a sagittal slice centered at the sonication site for each condition. Each individual animal was registered to each other by the minimal FDG uptake within the sonication site. (**F**) Estimated full-width at half-maximum (FWHM) of the sonication-induced changes in FDG avidity for each condition, and for the transducer used in these experiments. Presented are mean ± S.E.M. for groups of N=5–7. **: $p<0.01$ by two-tailed t-tests.

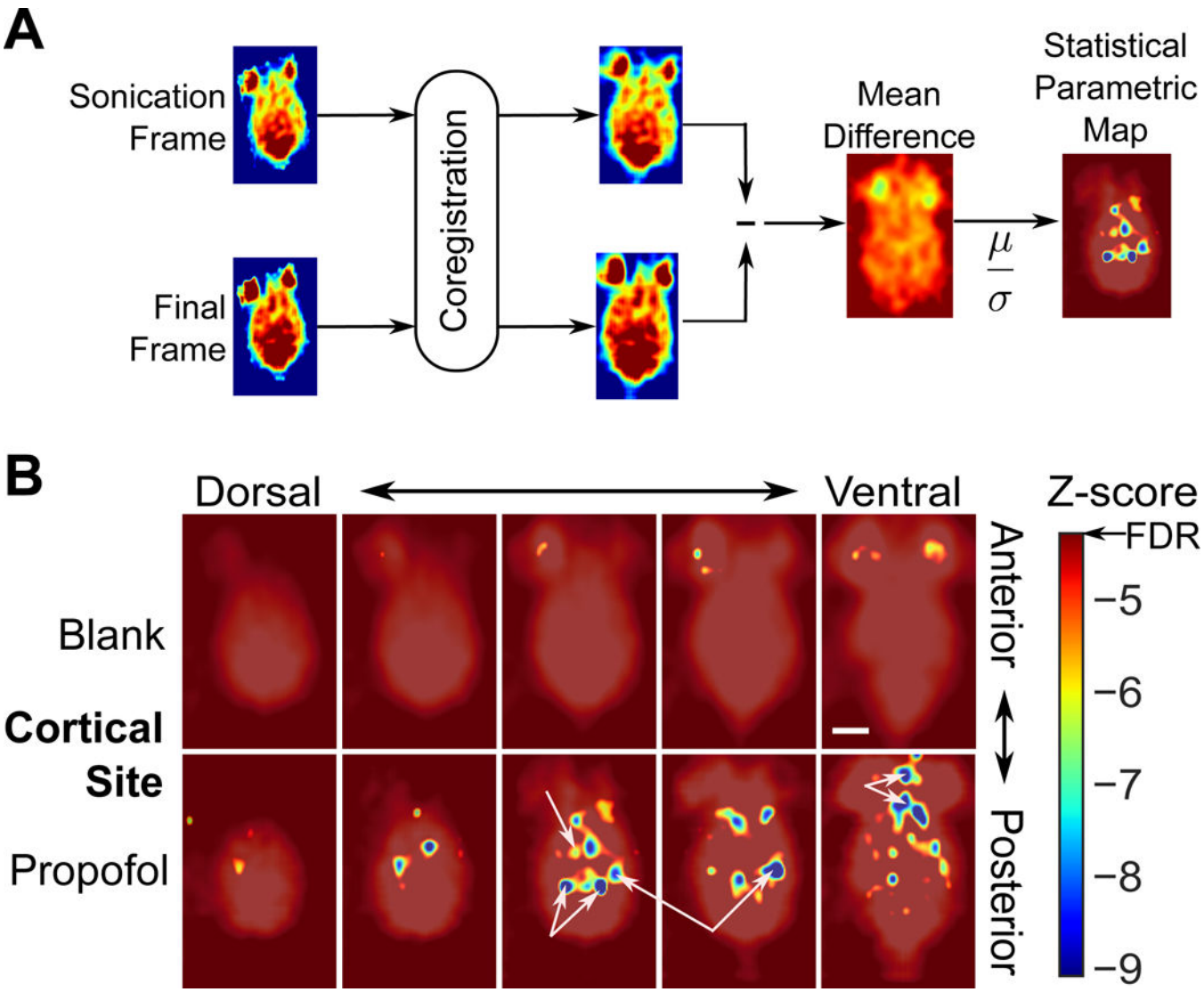

Fig. 4: Ultrasonic propofol uncaging maps functional connectivity of a cortical target.

(**A**) Analysis scheme for statistical parametric mapping of the whole-brain effects of targeted ultrasonic propofol uncaging. Following whole-brain coregistration, FDG PET frames during sonication and at the end of the acquisition were subtracted. This difference was averaged across animals, divided by the standard error across each group on a voxel-by-voxel basis, and thresholded at the false discovery rate (FDR), producing a z-score statistical parametric map. (**B**) Functional connectivity maps for cortical target sonication of animals receiving blank (*top*) or propofol-loaded (*bottom*) nanoparticles. Unannotated map is provided in Fig. S4A-B. CT: Central thalamus, Tc/PT: Tectum/posterior thalamus, H: Hippocampus, O: Olfactory bulbs and cortex.

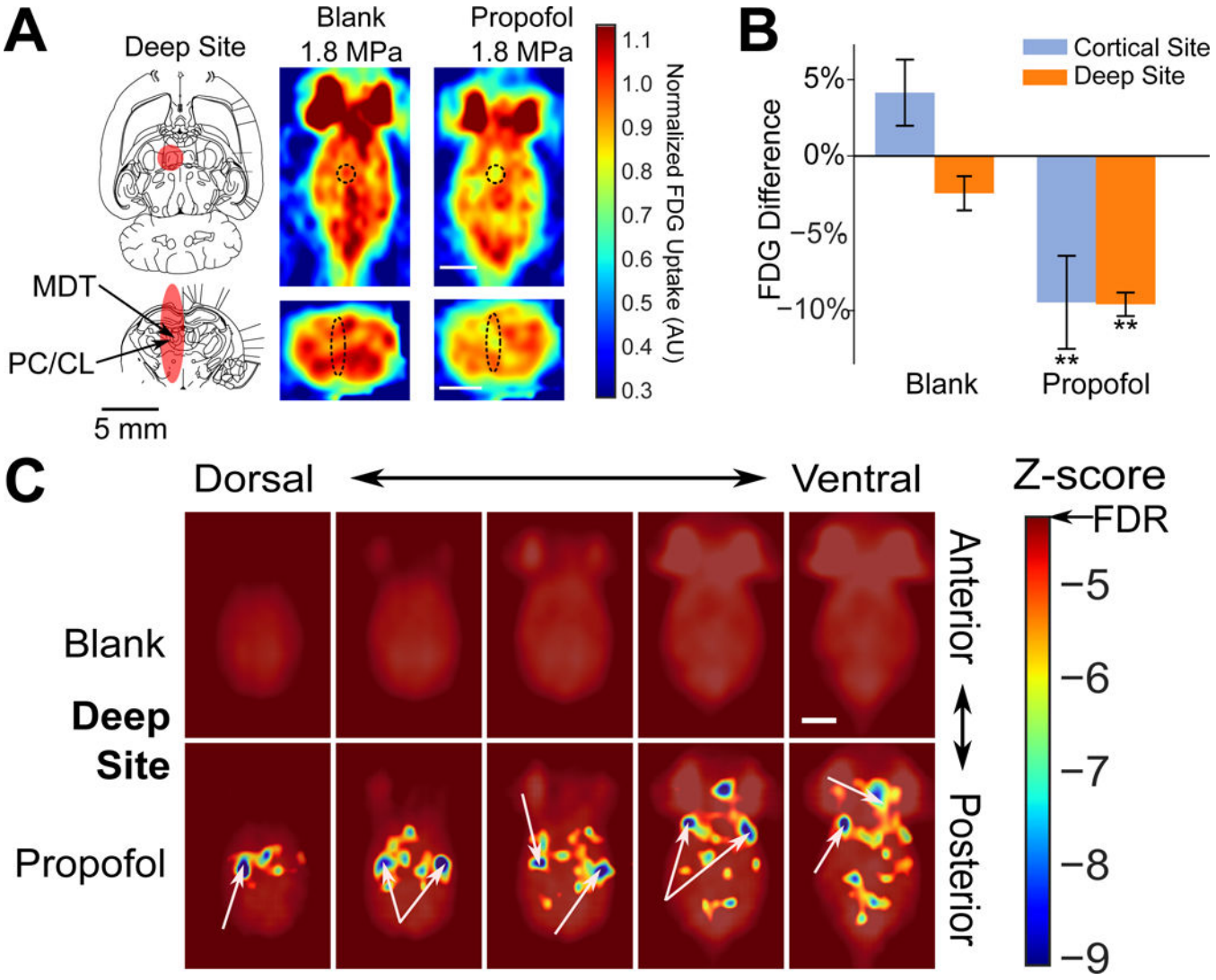

Fig. 5: Ultrasonic propofol uncaging in deep structures yields a unique functional connectivity signature.

(**A**) *Left*: Deep sonication target FWHM (red) overlaid onto transverse (*top*: −5.6 mm ventral to bregma) and axial (*bottom*: −3 mm caudal to bregma) rat atlas sections (Paxinos and Watson, 2013). MDT: mediodorsal thalamus, PC/CL: paracentral/centrolateral nuclei of the thalamus. *Right*: Individual animal transverse (*top*) and axial (*bottom*) PET images obtained during sonication (60 × 50 ms bursts at 1 Hz burst frequency, 1.8 MPa peak *in situ* pressure; black dashed ellipse: expected sonication FWHM), following blank or propofol-loaded nanoparticle administration. Color bar represents FDG uptake, normalized against the average FDG uptake in the contralateral hemisphere. Scale bars: 5 mm. **(B)** Quantification of FDG avidity difference during sonication in the sonication field minus the contralateral non-sonicated field following blank or propofol-loaded nanoparticle administration for either cortical (repeated from Fig. 3 for ease of comparison) or deep target sonication. Presented are mean +/− S.E.M. for groups of N=6–7. **: $p<0.01$ by two-tailed t-tests. (**C**) Functional connectivity maps for deep target sonication of animals receiving blank or propofol-loaded nanoparticles. Unannotated map is provided in Fig. S4C. FC: Frontal

cortex, LT: Lateral thalamus, TeA: Tegmental association area, I: Insula, O: Olfactory bulbs and cortex.

Key Resources Table

REAGENT or RESOURCE	SOURCE	IDENTIFIER
Chemicals, Peptides, and Recombinant Proteins		
mPEG-PLGA (Mw: 2,000:5,000 Da)	Akina	AK090
Propofol	Alfa-Aesar	L06841; CAS: 2078–54–8
Ketamine Hydrochloride	Stanford University Environmental Health & Safety	CAS: 1867–66–9
Tetrahydrofuran (THF)	Sigma-Aldrich	401757; CAS: 109–99–9
Hexane	Sigma-Aldrich	296090; CAS: 110–54–3
n-Perfluoropentane (PFP)	FluoroMed	APF-30M; CAS: 678–26–2
MultiHance Gadobenate Dimeglumine	Bracco Diagnostics	0270–5164; CAS: 127000–20–8
[18F]-Fluorodeoxyglucose (FDG)	Stanford Cyclotron	CAS: 105851–17–0
Microbubbles	Lantheus	Definity (DE4)
IRDye 800RS	LI-COR Biotechnology	IR800
Experimental Models: Organisms/Strains		
Rats; Long-Evans Wild-Type	Charles River	Strain ID: 006
Software and Algorithms		
Python v3.6	Anaconda	https://www.anaconda.com/download/
ImageJ (Fiji)	Schindelin, J et al., 2012	https://imagej.net/Downloads
Simple ITK Python Package v4.12.12	ITK	https://itk.org/ITK/resources/software.html
Data Acquisition and Analysis code	This paper	Available upon request
Other		
Focused Ultrasound System: Integrated Generator, RF Amplifier, Circulation System, and Transducer (2x)	Image Guided Therapy	Custom model
Stereotactic Frame	Image Guided Therapy	Custom model
Bath Sonicator	Thermo Scientific	Bransonic M1800H
Membrane Extruder	Avestin	Liposofast LF-50
Zetasizer	Malvern Panalytical	Zetasizer Nano ZS90
Microtiter Plate Reader	Tecan	Infinite M1000 PRO
Fluorescent Imaging System	Spectral Instruments Imaging	Lago Part #: A1666
3T MRI	MR Solutions	MRS 3017
EEG Recording Board	OpenBCI	Cyton
USB Breakout Board	Adafruit	FT232H
USB Isolator	Adafruit	2107
Green LED	Linrose	B4304H5–10
Raspberry Pi	RS Components Ltd	RPi 2 Model B

REAGENT or RESOURCE	SOURCE	IDENTIFIER
PET Scanner	Concorde Microsystems	MicroPET R4